Polylactic acid electrospun membranes coated with chiral hierarchical-structured hydroxyapatite nanoplates promote tendon healing based on a macrophage-homeostatic modulation strategy

Gang Luo [a,b,1], Juehong Li [a,b,1], Shuai Chen [a,b], Zhengqiang Yuan [a,b], Ziyang Sun [a,b], Tengfei Lou [a,b], Zhenyu Chen [a,b], Hang Liu [a,b], Chao Zhou [a,b,*], Cunyi Fan [a,b,**] , Hongjiang Ruan [a,b,***]

[a] *Department of Orthopaedics, Shanghai Sixth People's Hospital Affiliated to Shanghai Jiao Tong University School of Medicine, 600 Yishan Rd, Shanghai, 200233, PR China*
[b] *Shanghai Engineering Research Center for Orthopaedic Material Innovation and Tissue Regeneration, Building 3, Langu Science and Technology Park, Lane 70, Haiji 6th Road, Shanghai, PR China*

ARTICLE INFO

ABSTRACT

Tendon injury is a common and challenging problem in the motor system that lacks an effective treatment, affecting daily activities and lowering the quality of life. Limited tendon regenerative capability and immune microenvironment dyshomeostasis are considered the leading causes hindering tendon repair. The chirality of biomaterials was proved to dictate immune microenvironment and dramatically affect tissue repair. Herein, chiral hierarchical structure hydroxylapatite (CHAP) nanoplates are innovatively synthesized for immunomodulatory purposes and further coated onto polylactic acid electrospinning membranes to achieve long-term release for tendon regeneration adaption. Notably, levorotatory-chiral HAP (L-CHAP) nanoplates rather than dextral-chiral or racemic-chiral exhibit good biocompatibility and bioactivity. In vitro experiments demonstrate that L-CHAP induces macrophage M2 polarization by enhancing macrophage efferocytosis, which alleviates inflammatory damage to tendon stem cells (TDSCs) through downregulated IL-17-NF-κB signaling. Meanwhile, L-CHAP-mediated macrophage efferocytosis also promotes TDSCs proliferation and tenogenic differentiation. By establishing a rat model of Achilles tendon injury, L-CHAP was demonstrated to comprehensively promoting tendon repair by enhancing macrophage efferocytosis and M2 polarization in vivo, finally leading to improvement of tendon ultrastructural and mechanical properties and motor function. This novel strategy highlights the role of L-CHAP in tendon repair and thus provides a promising therapeutic strategy for tendon injury.

1. Introduction

Tendon, a distinctive mechanosensitive tissue connecting muscle to bone, primarily functions to transmit the force generated by muscle contraction to the bone, enabling body movement [1]. Composed of collagen fibers, tenocytes, and tendon stem/progenitor cells, tendon possesses remarkable tensile strength and durability, capable of withstanding the substantial forces exerted during muscular contraction [2]. Tendon injury is a common musculoskeletal pathology, usually followed by acute overload, tearing, overuse, or age-related degeneration, which results in severe pain and dysfunction, and greatly increases the burden on society and family [3–5]. Existing clinical treatments used for tendon repair include drugs, surgery, physical therapy, and rehabilitation [6]. However, Tendon repair after injury is a complex and

---

poorly understood process. Common complications after therapeutic intervention, including peritendinous adhesion, scarring, retear and restricted range of motion affect tendon repair. Restoring the native structure and function of injured tendons post-therapy remains a prevalent clinical challenge [6,7].

Macrophages perform various roles in tissue healing, including host defense, phagocytosis, growth factors production, and secretion of both pro-inflammatory and anti-inflammatory mediators [8–10]. The response to tendon injury can be divided into three overlapping stages, namely the inflammatory stage, repair stage, and remodeling phase [11]. The macrophage phenotype exhibits an intricate dual role in the inflammatory and repair stages of tendon healing. Macrophages have a spectrum of different functional phenotypes, including the M1 phenotype with a pro-inflammatory response, and the M2 phenotype associated with the resolution of inflammation and structural tissue healing [12]. In the specific immune microenvironment of tendon injury, the M1/M2 balance of the macrophage immunophenotype is disrupted, and impaired macrophage function may be the most crucial reason for aberrant tendon repair [13]. At the same time, previous studies suggest that lack of inflammation and polarization of M2 macrophage were more favorable factors in regenerative healing. Therefore, macrophage function phenotype appears to play a key role in the development of improved therapies for tendon healing.

With the advancement of materials chemistry and the deep integration of medicine and engineering, the biological properties of many materials have been uncovered and reported for the regulation and treatment of immune responses in relevant diseases [14–17]. Chirality is a ubiquitous phenomenon in nature and living organisms, playing important roles in many physiological processes [18]. Previous research has shown that chiral biomaterials can effectively regulate cell behaviors such as adhesion, proliferation, and differentiation [19]. Moreover, chiral biomaterials have shown promising and positive effects in specific disease models, including peripheral nerve injury, skin wounds, tendon-to-bone healing, and tumors [20]. For example, Cai et al. [21] developed hierarchical chiral calcium silicate hydrate films and found that the levorotatory chiral calcium silicate hydrate film could facilitate angiogenesis of endothelial cells to promote revascularization at the enthesis for tendon-to-bone healing. Zhu et al. [22] reported that the dextral chiral hydrogel could enhance cell proliferation and promote diabetic wound healing. However, data on using chirality to optimize biomaterials as an immunocyte regulation strategy are still lacking, especially in tendon. Xu et al. [23] first reported that different chiral gold bionic nanoparticles exhibited different immune responses both in vitro and in vivo, and found that L-P⁺ nanoparticles, as an adjuvant mixed with H9N2 influenza vaccine to immunize mice, could significantly enhance the proliferation of immune cells, reduce inflammatory responses and tissue damage, which provided possibilities for subsequent researchers to further explore the potential immunomodulatory functions of chiral materials in other disease fields. Therefore, it is highly desirable to investigate the effects of biomaterial chirality on macrophage function and uncover the related biological mechanisms during tendon regeneration.

The materials currently used for enhancing tendon repair can be classified into two major categories: collagen-based materials and xenografts, including collagen, fibrin, hyaluronic acid, elastin, alginate, chitosan, porcine small intestinal submucosa, human or animal dermis, and acellular tendon xenografts [1]. However, these materials are still beset with some deficiencies such as lack of adapted degradation rate, poor biological activity, immune rejection, and poor mechanical properties. Hydroxyapatite (HAP), as a green catalyst and one of the main inorganic components of human and animal musculoskeletal systems, shows good biocompatibility and bioactivity [24], and has been documented to regulate immune microenvironment and macrophage polarization in tissue regeneration [25,26]. Taking these factors into account, chiral hydroxyapatite is an appropriate component for creating chiral biomaterials for tendon repair. To achieve long-term sustained release of

chiral hydroxyapatite for tendon regeneration adaption, a suitable carrier for sustained-release materials is essential. Polylactic acid (PLA) has been widely utilized in biomaterials over the past decades due to its excellent properties, including easy processing, low immunogenicity, good biocompatibility, and biodegradability [27]. Combining the advantages of electrospun membranes including versatility, simplicity, high porosity, and large surface area-to-volume ratio [28], PLA electrospun membranes can be used as a high-quality carrier for various materials acting on tissues and cells.

Herein, we originally designed L-/D-/Racemic-chiral hierarchical structure hydroxyapatite nanoplates coated on a PLA electrospinning membrane (CHAP@PLA) based on a facile chiral malic acid (MA) molecules induced self-assembly strategy (Scheme 1). In vitro experiments demonstrated that L-CHAP@PLA had excellent biocompatibility and bioactivity, and could promote immune homeostasis modulation and tenogenic differentiation ability by enhancing macrophage efferocytosis. In a rat model of Achilles tendon injury, L-CHAP@PLA mediated macrophage efferocytosis modulated M1/M2 polarization rate and increased the expression of markers related to tendon and collagen remodeling, leading to improvements in structural, functional and mechanical properties of the tendon. These results validated the promoting effect of L-CHAP@PLA on tendon healing, providing a promising therapeutic avenue for tendon injury patients.

2. Results and discussion

2.1. Synthesis of CHAP@PLA

We deposited chiral hierarchical structure hydroxyapatite (CHAP) nanoplates on a PLA electrospinning membrane based on a facile chiral MA molecules-induced self-assembly strategy (Fig. 1a). Briefly, after the preparation of PLA substrate and elimination of contaminants, the CHAP nanoplates were evenly settled onto PLA from a homogeneous solution that comprised MA, simulated body fluid, pH regulator and deionized water under biomineralization conditions. The decision to employ L-/D-/Racemic-MA was based on its dual role as a structural director and symmetry disruption catalyst during the asymmetric binding and mutual assembly procedure involving calcium ions, leveraging its coordination properties. The pH value of the reaction system is controlled by acid-base regulator, which in turn controls nucleation rate and crystal growth rate. During the reaction, chiral MA molecules coordinate with calcium ions to form a complex. After being mixed with phosphate ions and urea under heating, the phosphate ions gradually replace the MA
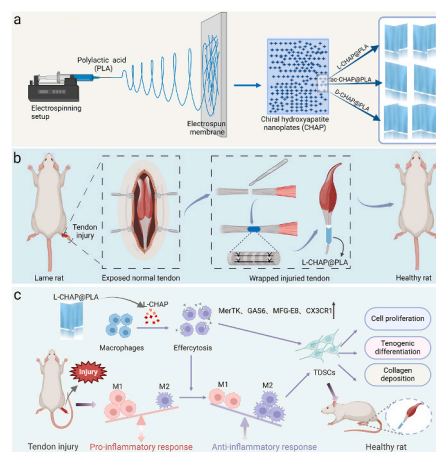
Scheme 1. Schematic illustration of chiral CHAP films mediated macrophage-homeostatic modulation for tendon healing. a) Preparation of chiral CHAP films. b) Implantation of L-CHAP@PLA promoting tendon repair. c) Schematic illustration depicting the mechanism of chirality-dependent macrophage-homeostatic modulation.
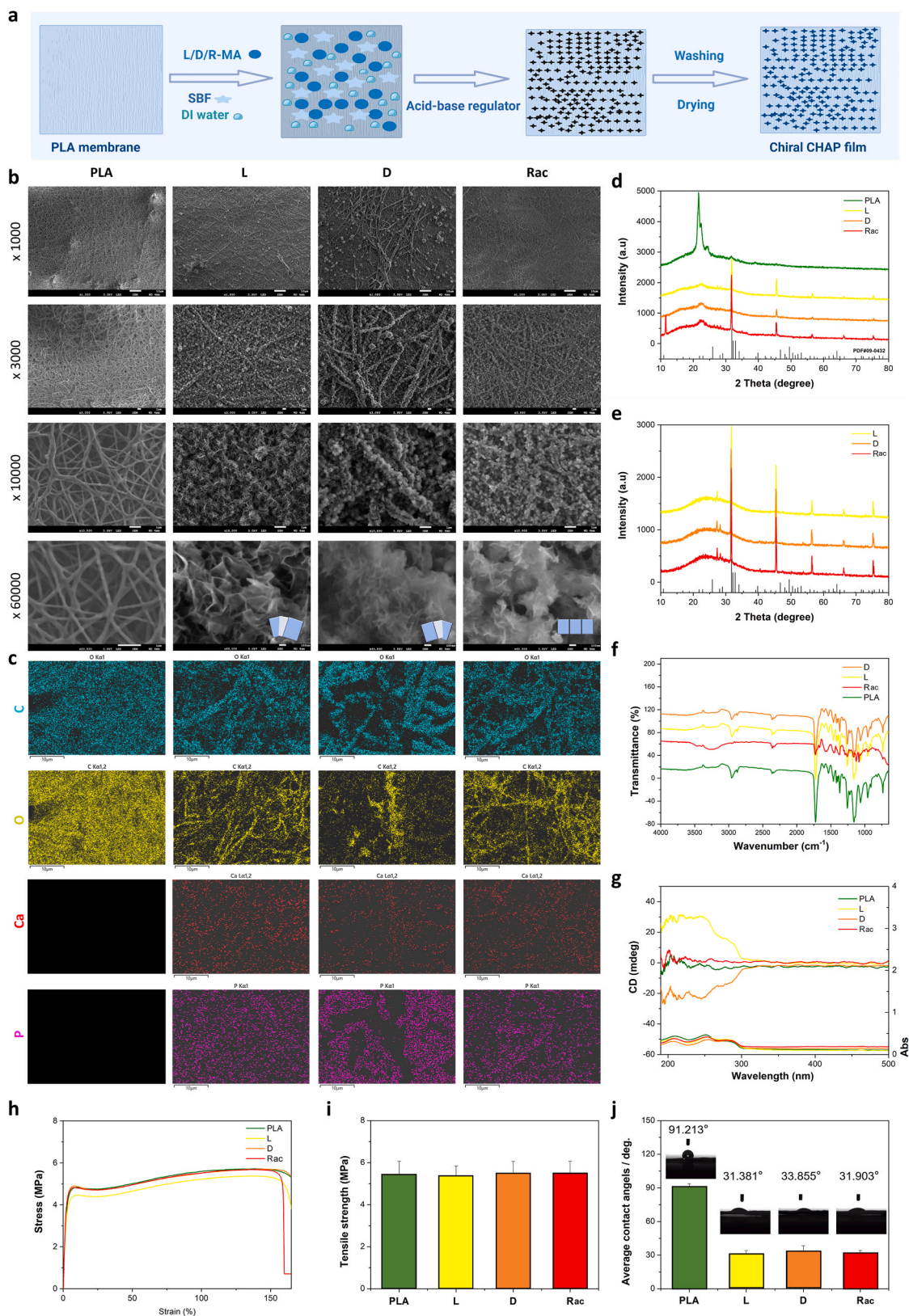
Fig. 1. Morphological, structural, physical and chemical properties of CHAP@PLA. a) Schematic drawing of the synthetic process of chiral CHAP membranes. b) SEM images and diagram of PLA, L, D and Rac at varying magnifications, respectively. (note, the maximum magnification of PLA is ×20000, L, D and Rac is x60000). c) EDS mapping of PLA, L, D and Rac, Scale bar, 10 μm. The synthetic composition was 0.2 mmol MA, 20 mL 5M SBF, x mL HCl or Tris, pH = 6.4, 20 mL H₂O. d)XRD patterns of PLA substrate and CHAP@PLA. e) XRD patterns of corresponding HAP powder, λ_{Cu} = 1.5418 Å, HAP JCPDS cards. No. 09–0432. f) FTIR of the PLA, L, D and Rac. g) DRUV-Vis and DRCD spectra of the antipodal PLA@CMHAP shown in Fig. 1a, measured with white background. h) and i) Stress-strain curve and tensile strength of the PLA, L, D and Rac, respectively. j) Contact angles of the PLA, L, D and Rac (n = 3).

molecules, and then mineralization and crystallization occur to form hydroxyapatite. Due to the chiral spatial imprint left by the chiral MA molecules, the arrangement of atoms in all the formed hydroxyapatite crystals retains the chiral imprint, ultimately facilitating chiral molecules to achieve the formation of an asymmetric crystal (chiral HAP nanosheets) structure. Retrieving the PLA substrate from synthesis solution to collect CHAP@PLA nanoplates, which were used for tendon injury repair material. The CHAP@PLA membranes synthesized with L-MA, D-MA, and Racemic-MA were abbreviated as L, D, and Rac, respectively.

2.2. Morphological, structural, physical and chemical property characterizations of CHAP@PLA

The antipodal L and D membranes are white with a fibrous reticular structure. Fig. 1b shows the ultrastructural images of PLA, L, D and Rac membranes by scanning electron microscopy. It can be observed that PLA displays a network porous structure composed of nanofibers, while CHAP showcases a floral morphology with aggregated nanosheets located on the surface of PLA membranes. On L membrane, the L-CHAP flowers are consisted of dense arrays of nanoplates with widths of 50~200 nm, thicknesses of 10~20 nm and heights of 0.1–1 μm grown on the surface of the PLA membranes. Analogously, the right-handed helical configuration can also be detected in D-CHAP flower on D membranes (Fig. 1b). An enlarged SEM image elucidates the wave-twisting pattern of the nanoplates, indicative of the secondary chirality present in the D-CHAP formation. As reported in our previous study [29], the primary chirality results are also right-handed. The Rac-CHAP flower on Rac membranes (Fig. 1b) shows that nanoplates are randomly arranged and exhibit an irregular structure, and therefore does not show a chiral multilevel structure. Energy-dispersive X-ray spectroscopy (EDS) mapping of the PLA substrate and the L, D, and Rac-CHAP coatings demonstrates a uniform distribution of calcium, phosphorus, oxygen, and carbon elements across all coatings (Fig. 1c).

Wide-angle X-ray diffractometry (XRD) was utilized to delve into the structural attributes of the PLA, L, D, and Rac membranes. Despite the stronger intensity of the PLA substrate existed in the XRD pattern of L, D and Rac membranes, the reflections of the characteristic reflection of the hexagonal phase of CHAP with the space group $P6_3/m$ with lattice parameters of a = b = 9.4166 Å and c = 6.8745 Å remain distinguishable (Fig. 1d). Furthermore, the corresponding powder was also examined, and the spectrogram results showed that the characteristic peaks of strong hydroxyapatite appeared in the powder (Fig. 1e). At the same time, a certain steamed bun peak is also found in the low-angle area, indicating that the hydroxyapatite powder contains some components with a low degree of crystallization.

The reliability of PLA, L, D and Rac membranes was demonstrated utilizing Fourier-transform infrared spectroscopy (FTIR). Fig. 1f showed that bands at 961 cm^{-1} reflected qvl PO$_4^{3-}$, and 1125 cm^{-1} forv PO$_4^{3-}$. The weak intensities of the OH stretching and libration were at 3426 and 637 cm^{-1} respectively. In the spectrum, bands positioned at 874 and within the range of 1420–1470 cm-1 are indicative of B-type carbonate apatite, characterized by the replacement of phosphate ions by carbonate ions within the crystal lattice structure of hydroxyapatite. The distinct chirality of the PLA, L, D and Rac membranes was accomplished through the examination of optical activity (OA), as evidenced by the application of diffuse reflectance ultraviolet–visible (DRUV-Vis) and circular dichroism (DRCD) spectroscopy as depicted in Fig. 1g. The left-handed structure preferentially absorbs right-handed circularly polarized light and reflects left-handed light, leading to negative absorption and scattering-based optical activity (OA) signals in the DRCD measurement. In terms of DRUV-Vis, the L and D membranes showed mirror-imaged signals at 190–310 nm as shown in Fig. 1h. The results of L membranes revealed that three broad bands in the UV–Vis spectrum in the range of 200–225 nm, 225–265 nm, and 265–310 nm, respectively, and three intense peaks in the CD spectrum at 218 nm, 250 nm and 285

nm were observed. Based on the detection mechanism, the OA of L membranes include SOA due to PLA substrate being seen as a white background. The mirror-imaged DRCD spectrum of D membrane indicates the opposite handedness. The DRCD spectra of PLA substrate confirmed that the OAs of L and D membranes arose from hierarchical chiral structures instead of PLA substrates. Rac membrane showed a similar morphology to antipodal CHAP flower but without chirality.

Mechanical performance is one of the dominant factors for tissue-engineered tendon repair materials. We investigated the stress-strain behavior of PLA, L, D, and Rac membranes. As shown in Fig. 1h, PLA, L, D and Rac showed similar stress and elongation, which proved that the mineralized chiral hydroxyapatite coating did not affect the strength and flexibility of PLA membrane. The results of tensile elongation at break are shown in Fig. S1, Supporting Information. In addition to stress-strain curve, tensile strength is shown in Fig. 1i, the results demonstrate that PLA, L, D and Rac have similar mechanical strength.

Fig. 1j shows that after passing through coating chiral hydroxyapatite, the hydrophilicity of PLA is greatly improved, and the contact Angle of PLA is reduced from the original 90°–30°, which is reduced by three times on the original basis. This lays a solid foundation for biocompatibility and biological applications.

2.3. Influence of CHAP@PLA on macrophages and TDSCs biocompatibility

Macrophages and TDSCs play crucial roles during the repair phase after tendon injury [12,30]. Therefore, the influence of CHAP@PLA on cells was evaluated on macrophages and TDSCs. Macrophages and TDSCs were seeded separately on PLA, L-CHAP@PLA, D-CHAP@PLA, and Rac-CHAP@PLA membranes. First, the morphology and arrangement of macrophages on PLA and L/D/Rac-CHAP@PLA membranes were explored using fluorescein–phalloidin and SEM (Fig. 2a). The macrophages treated with L-CHAP@PLA showed a more active cell morphology, and the cell spreading area in the L-CHAP@PLA group was larger than in the other groups. Subsequently, cell viability of macrophages was assessed quantitatively by CCK-8 assay (Fig. 2b and Fig. S2, Supporting Information). The results showed that on the first day of co-incubation with L/D/Rac-CHAP@PLA respectively, there was no substantial difference in the cell viability of the L/D/Rac-CHAP@PLA group compared with that of the control group, while D-CHAP@PLA group exhibited significantly poorer cell viability compared with the other groups on the third and fifth days. Cell compatibility was explored by AnnexinV/PI flow cytometry. Annexin V-positive cells indicate apoptotic macrophages, and the higher the proportion, the poorer the compatibility of the membrane with macrophages. Our results showed few apoptotic or necrotic macrophages cultured on L/Rac-CHAP@PLA membranes, reflecting good compatibility like the control group. In contrast, the D-CHAP@PLA membrane showed significantly poorer compatibility with macrophages than the control and L/Rac-CHAP@PLA groups (Fig. 2c–d).

Furthermore, we also explored the influence of CHAP@PLA on TDSCs behaviors. First, the proliferative capability of TDSCs was determined by 5-ethynyl-2′-deoxyuridine (EdU) incorporation assay (Fig. 2e–f) and CCK-8 assay (Fig. S3, Supporting Information). The incorporation of EdU can be used to track DNA replication progress, quantitatively reflecting the proliferation ability of TDSCs on CHAP@-PLA membranes. Our EdU incorporation assay results showed that DNA replication occurred more frequently in the L-CHAP@PLA group than in other groups, while the D-CHAP@PLA group showed a remarkable decrease in the number of EdU-positive cells compared to the control group. Moreover, the results from the Rac-CHAP@PLA and control groups showed no statistical significance. Similarly, the CCK-8 results showed that TDSCs cultured on L-CHAP@PLA were more proliferative than those on the control, Rac-CHAP@PLA and D-CHAP@PLA at day 3 and day 5. The live/dead staining assay was performed to assess TDSCs viability (Fig. 2g). The results indicated that the PI/calcein-AM cell rate
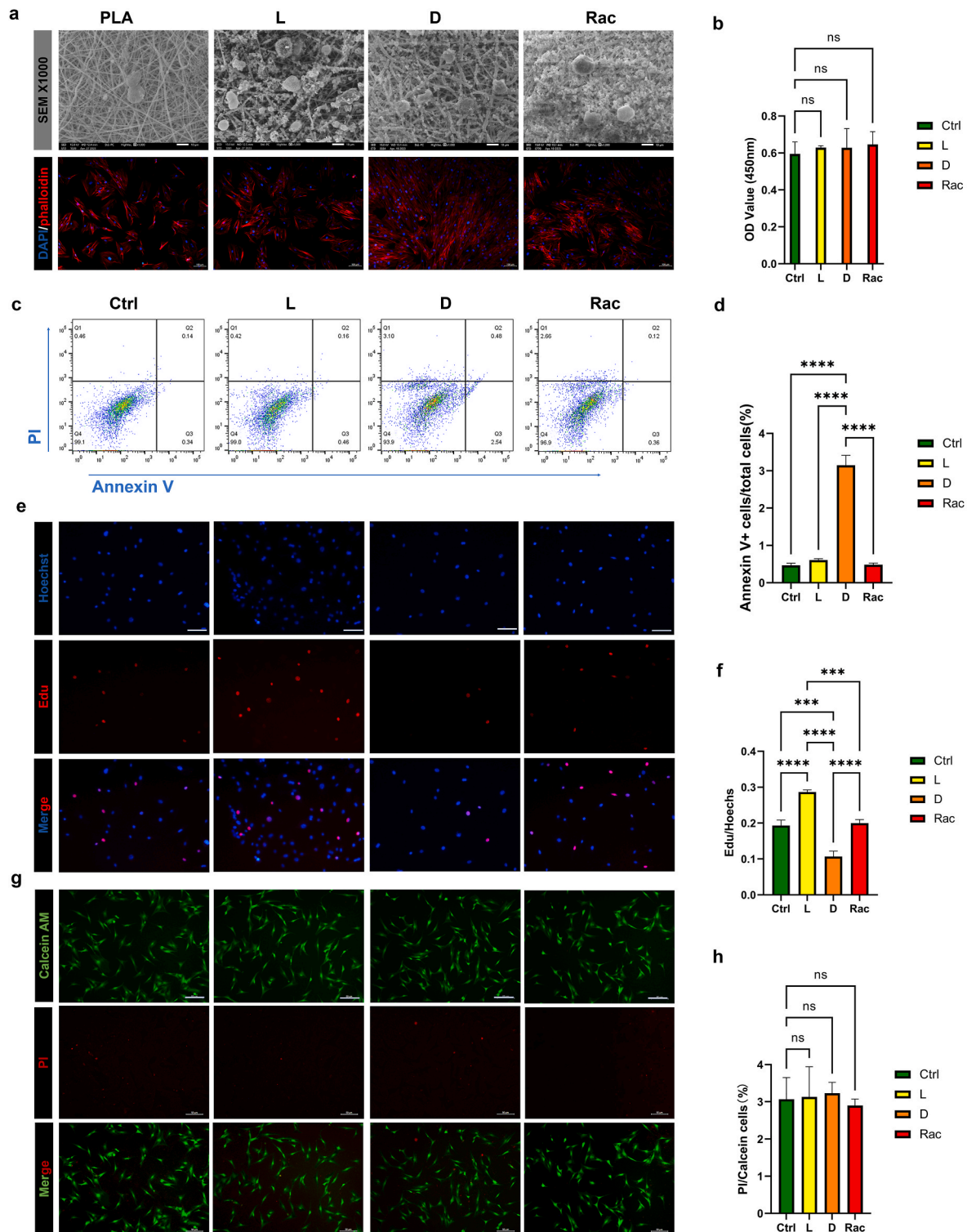
Fig. 2. Influence of CHAP@PLA on adhesion, viability, and proliferation of macrophages and TDSCs. a) SEM and immunofluorescence staining images of macrophages on the surface of PLA, L-CHAP@PLA, D-CHAP@PLA, and Rac-CHAP@PLA after incubating for 24 h (n = 5). b) Cell viability analysis of macrophages under L/D/Rac-CHAP@PLA tested by CCK-8 after incubating for 24 h (n = 5). c) Annexin V-PI flow cytometry results of macrophages cultured on control, L-CHAP@PLA, D-CHAP@PLA and Rac-CHAP@PLA. d) Statistic analysis of Annexin V+ cells/total cells rate of the control, L-CHAP@PLA, D-CHAP@PLA and Rac-CHAP@PLA groups. e) Representative fluorescent images showing Edu in TDSCs (n = 5). f) Statistic analysis of Edu/Hoechs rate of the control, L-CHAP@PLA, D-CHAP@PLA and Rac-CHAP@PLA groups (n = 5). g) Representative live/dead staining images of the control, L-CHAP@PLA, D-CHAP@PLA, and Rac-CHAP@PLA groups (n = 5). scale bar: 50 μm. h) Statistic analysis of dead/live cell rate of the control, L-CHAP@PLA, D-CHAP@PLA and Rac-CHAP@PLA groups. ns means not significant, ***p < 0.001, ****p < 0.0001, indicates significant differences between the two groups.

was consistent across all four groups, with no significant differences observed (Fig. 2h).

The enantiomers of chiral substances have the basically same physical properties (such as melting point, boiling point, density, etc.) in an achiral environment. However, in a chiral environment, there are differences in some physical properties between enantiomers. For example,

they have opposite optical activities and different odors. Meanwhile, diverse chiral structures also exert differential impacts on the behaviors of cells, which are predominantly manifested in aspects like cell adhesion and proliferation, cell differentiation, cell migration, as well as cytotoxicity [31]. For instance, left-handed nanofibers constructed from L-amino acid derivatives are capable of augmenting cell adhesion and
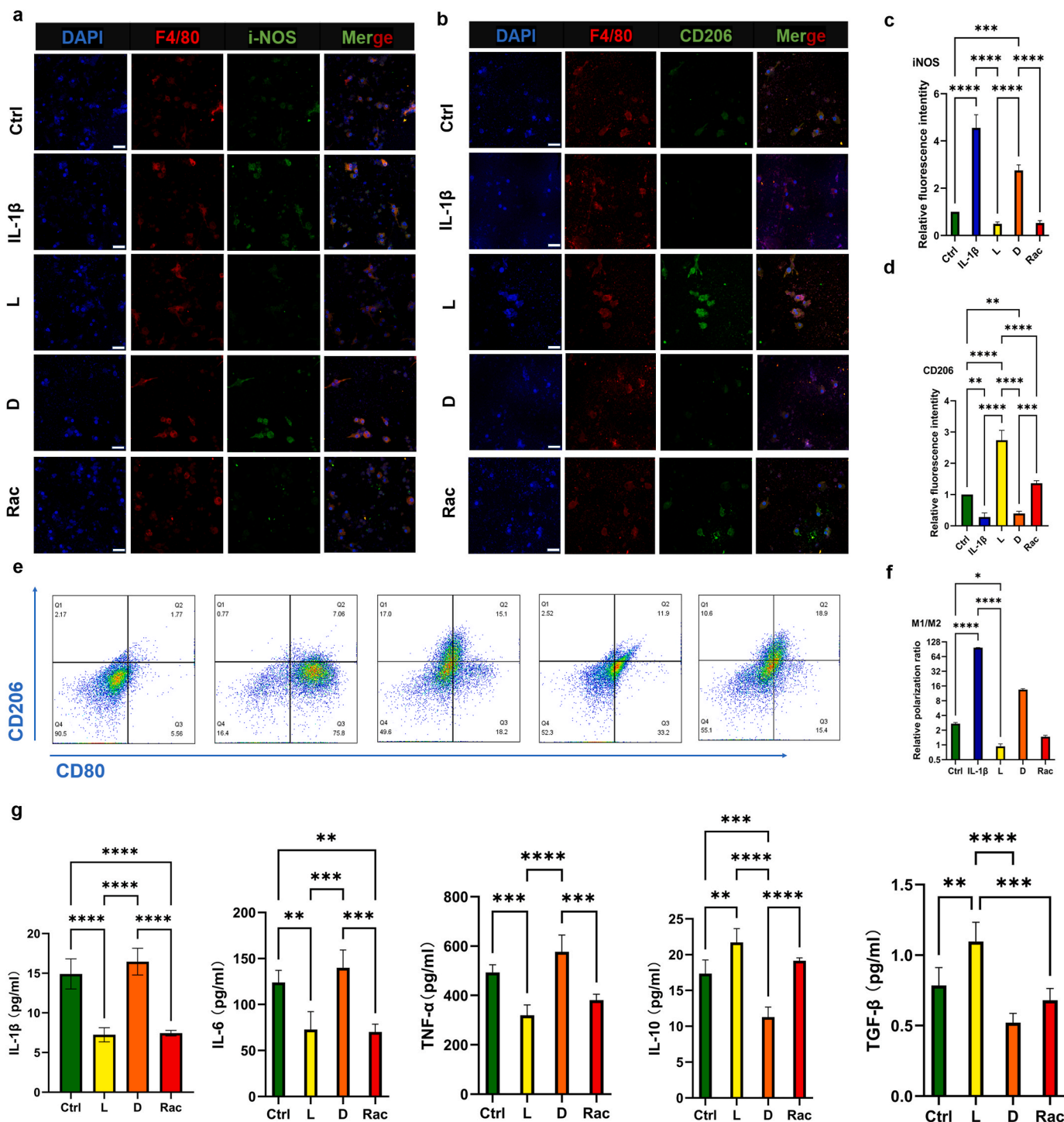

Fig. 3. Modulation on immune polarization of macrophages by L-CHAP@PLA in vitro. Representative immunofluorescence images of macrophage a) F4/80 (red) and i-NOS (green) and b) F4/80 (red) and CD206 (green) after co-incubation with control group, IL-1β group, IL-1β + L-CHAP@PLA group, IL-1β + D-CHAP@PLA group, and IL-1β + Rac-CHAP@PLA group. Scale bar, 20 μm. Corresponding relative fluorescence intensity quantification of c) i-NOS and d) CD206. e) Flow cytometry of macrophages CD80 (M1) and CD206 (M2) after co-incubation with each group and f) quantification of the corresponding percentage of positivity. g) Macrophage polarization-related cytokine expression was detected by ELISA, including IL-1β, IL-6, TNF-α, IL-10, and TGF-β (n = 5). *p < 0.05, **p < 0.01, ***p < 0.001, ****p < 0.0001, indicates significant differences between the two groups.

proliferation, while right-handed nanofibers originating from D-amino acids tend to impede cell adhesion and proliferation [32]. L-phenylalanine-based chiral nanofibers can induce retinal progenitor cells to differentiate into retinal neurons, whereas D-phenylalanine-based chiral nanofibers lead to differentiation into glial cells [33]. Flavonoid hydrogels with an L-chiral structure can enhance cell migration and serve as tissue regeneration scaffolds for wound healing, thereby facilitating the healing process [34]. Moreover, exogenously administered L-RNA has potential cytotoxicity, and its toxicity depends on factors such as the chemical structure of the backbone, sequence, and structure [23]. In this study, L-CHAP@PLA showed a superior level in biocompatibility experiments with macrophages and TDSCs compared to Rac-CHAP@PLA and D-CHAP@PLA.

2.4. L-CHAP@PLA-modulated immune homeostasis of macrophage function

To further elucidate the impact of CHAP@PLA on macrophages homeostasis, a series of experimental groups were established, including the control group, interleukin-1β (IL-1β) group, where IL-1β was used to simulate an inflammatory microenvironment), L-CHAP@PLA group (L-CHAP@PLA combined with IL-1β), Rac-CHAP@PLA group (Rac-CHAP@PLA combined with IL-1β), and D-CHAP@PLA group (D-CHAP@PLA combined with IL-1β). Immunofluorescence (IF) staining assay was performed to observe the expression level of i-NOS (M1 marker) and CD206 (M2 marker). The results revealed that the i-NOS level in macrophages treated with L-CHAP@PLA was markedly diminished compared to the IL-1β group and similar to the control group, while the expression level of CD206 was found to be the highest among all four groups (Fig. 3a–d). Flow cytometry analysis revealed that L-CHAP@PLA treatment in the inflammation microenvironment
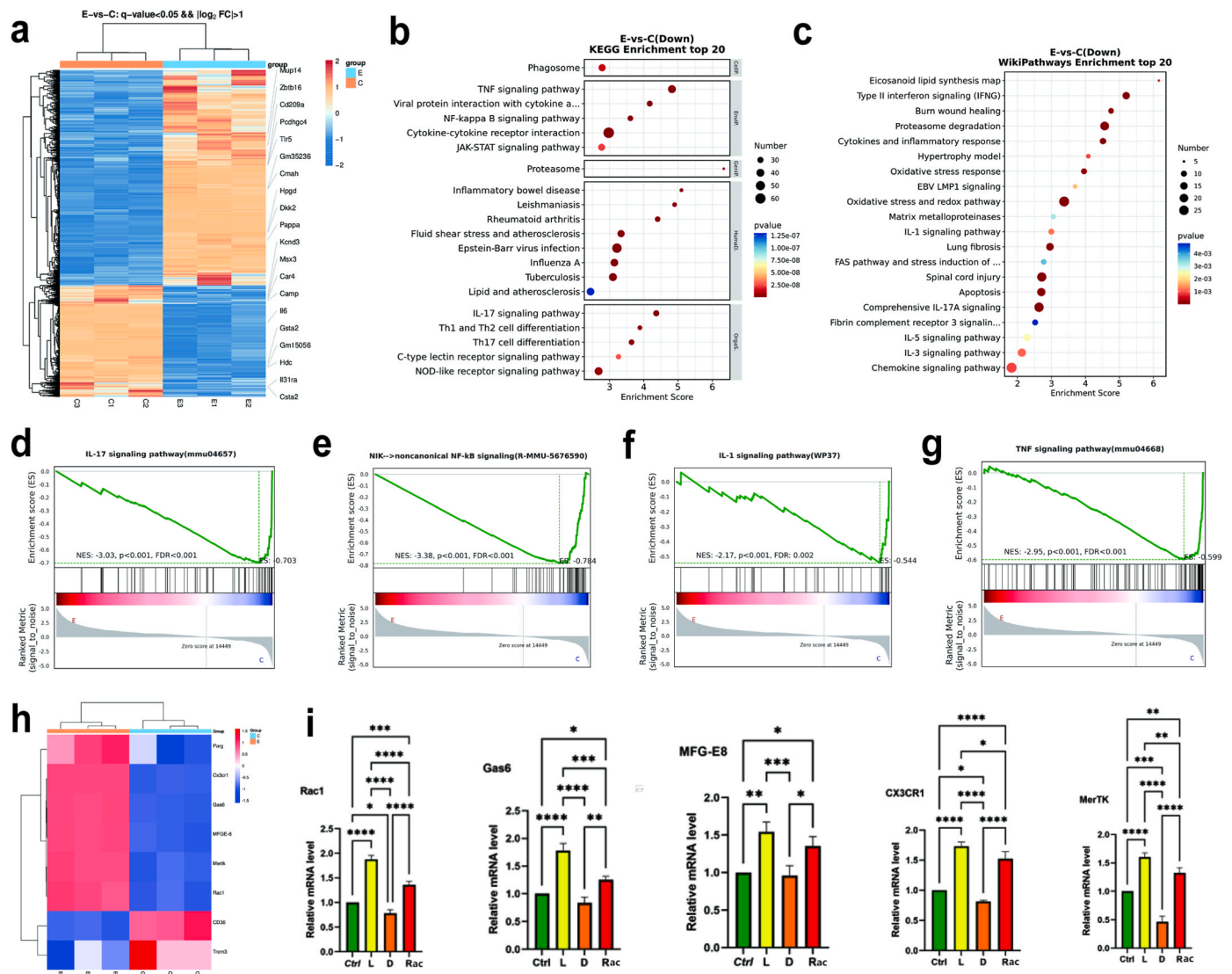

Fig. 4. Mechanisms of L-CHAP@PLA modulation of immune polarization of macrophages. a) Heat map of group differences in gene expression between the control and L-CHAP@PLA groups (n = 3). b) Top 20 of downregulated differential gene KEGG enrichment pathway for L-CHAP@PLA compared to control group. c) Top 20 of downregulated differential gene WikiPathway enrichment for L-CHAP@PLA compared to control group. GSEA enrichment analysis graphs of d) IL-17 signaling pathway, e) NF-κB signaling pathway, f) IL-1 signaling pathway, and g) TNF-α signaling pathway. h) Heat map of differential genes involved in the regulation of efferocytosis effect of macrophages by L-CHAP@PLA and control groups. i) Expression level of mRNA related to efferocytosis effect (Rac1, Gas6, MFG-E8, CX3CR1, and MerTK) of macrophages after co-incubation with each group (n = 5). *p < 0.05, **p < 0.01, ***p < 0.001, ****p < 0.0001, indicates significant differences between the two groups.

significantly decreased the M1/M2 ratio compared to both the IL-1β group and control group (Fig. 3e–f). Meanwhile, the immune-related cytokine expression in macrophages exposed to various CHAP@PLA membranes was assessed using enzyme-linked immunosorbent assay (ELISA) (Fig. 3g). The results indicated that the expression levels of pro-inflammatory cytokine IL-1β, IL-6, and TNF-α in macrophages treated with L-CHAP or Rac-CHAP@PLA were significantly downregulated compared to the control group. Conversely, the expression levels of IL-10 and TGF-β (cytokine associated with M2 macrophages) were notably augmented compared to the control group and D-CHAP@PLA group, suggesting that L-CHAP@PLA have the effect of regulating the immune function of macrophages by promoting M2 polarization of macrophages and weakening M1 polarization within the inflammation microenvironment, which was similar to previous reports on inflammatory regulatory function of hydroxyapatite [25]. In summary, our results initially demonstrated that L-CHAP@PLA downregulated the M1/M2 ratio to level in the inflammation microenvironment, reduced the expression of pro-inflammatory cytokines, promoted M2

polarization, and achieved homeostatic regulation of macrophage function. However, the specific mechanism by which L-CHAP@PLA achieves this function and the involved signaling axis warrant further exploration.

2.5. Mechanism of L-CHAP@PLA-Modulated immune homeostasis

To further explore the macrophage immune homeostatic mechanisms regulated by L-CHAP@PLA, transcriptomic mRNA analysis of macrophages was conducted to assess the overall effect of L-CHAP@-PLA. Quality control data, including PCA, FPKM values, and sample-to-sample distance, confirmed the stability of the mRNA-seq results by indicating favorable group variations (Fig. S4, Supporting Information). Following L-CHAP@PLA treatment, analysis via heatmap and volcano plot (Fig. 4a and Fig. S5, Supporting Information) revealed that 2674 genes were upregulated and 1385 genes were downregulated in macrophages compared to the control group. It is noteworthy that KEGG and WikiPathways enrichment analysis indicated that the IL-17, NF-κB, IL-1
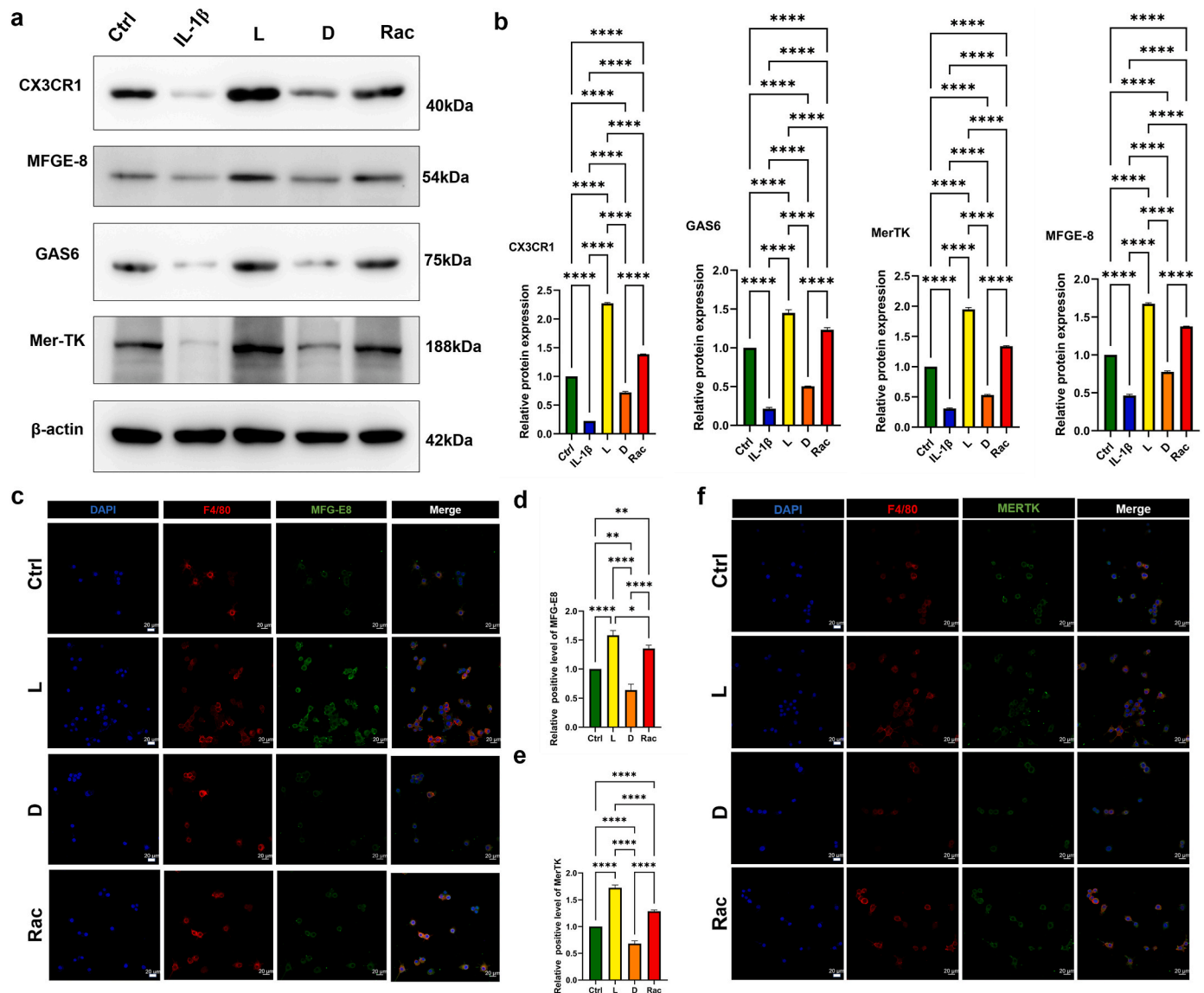

Fig. 5. The pro-efferocytosis effect of L-CHAP@PLA enhances the modulation of macrophage M2 polarization. a) Western blot analysis of efferocytosis effect proteins in macrophages after co-incubation with each group and b) the corresponding relative protein quantification. (n = 5). c) Representative immunofluorescence image of F4/80 (red) and MFG-E8 (green) in macrophages after co-incubation with each group. Scale bar, 20 μm. d) Corresponding relative fluorescence intensity quantification of MFG-E8 and e) MerTK. f) Representative immunofluorescence image of F4/80 (red) and MerTK (green) in macrophages after co-incubation with each group. *p < 0.05, **p < 0.01, ****p < 0.0001, indicates significant differences between the two groups.

and TNF signaling pathways were significantly downregulated in macrophages after L-CHAP@PLA intervention (Fig. 4b–g). These findings suggest that L-CHAP@PLA modulates macrophage immune function by downregulating inflammation-related signaling pathways, resulting in decreased release of inflammatory cytokines and chemokines, thus maintaining macrophage immune homeostasis.

Additionally, disparities in macrophage efferocytosis-related genes were also observed between the L-CHAP@PLA group and the control group (Fig. 4h). Efferocytosis, the process whereby cells engulf and eliminate apoptotic cells, is a crucial mechanism for preserving tissue homeostasis and warding off inflammation [35,36]. Current evidence indicates that numerous cells experience inflammatory apoptosis and necrosis within the trauma-induced inflammatory microenvironment. Unless these necrotic cells are cleared in time, they will continuously trigger inflammatory infiltration, leading to immune microenvironment imbalance and thus forming a vicious cycle. Enhanced efferocytosis is advantageous for the elimination of inflammatory apoptotic cells, thereby promoting wound healing [37]. Prior research has shown that improved macrophage efferocytosis enhanced bone repair and attenuated tendon injury-related heterotopic ossification formation by reversing inflammation and remodeling the macrophage immune homeostasis [38,39]. This study demonstrated that L-CHAP@PLA treatment significantly upregulated efferocytosis-related gene expression in macrophages, as confirmed by mRNA sequencing and qRT-PCR assays. Fig. 4 illustrates that macrophages treated with L-CHAP@PLA exhibit elevated expression levels of "find me" genes (MerTK, CX3CR1), "eat me" genes (MFG-E8, Gas6), and the endocytosis gene Rac1 compared to the control group. The protein expression trend of efferocytosis-related genes was consistent with that in mRNA expression (Fig. 5a–b). Additionally, immunofluorescence staining revealed increased expression of MFG-E8 and MerTK in macrophages treated with L-CHAP@PLA (Fig. 5c–f), indicating enhanced macrophage efferocytosis and downregulation of the inflammatory signaling axis.

Previous studies have demonstrated that macrophage efferocytosis has an important impact on the polarization tendency of macrophages. In a mouse model, it has been found that the efferocytosis function of macrophages with MerTK deficiency is impaired, leading to a persistent inflammatory response [40]. During the process of efferocytosis, some signal molecules related to the polarization of M2 macrophages are activated such as the STAT6 signaling pathway. The activated STAT6 signaling pathway promotes the expression of M2 macrophage marker genes arginase-1 [41]. It is widely known that M2 macrophages play a crucial role in the tendon repair process. They can secrete various growth factors that promote the proliferation, migration and differentiation of tendon cells, such as PDGF and VEGF. In addition, M2 macrophages can promote the remodeling and maturation of ECM by regulating the expression of ECM-related genes [42]. Therefore, we believe that macrophage efferocytosis, by regulating the M1/M2 polarization balance, not only can cause the inflammatory response to subside at an appropriate time point but also creates favorable conditions for the repair phase of tendon healing. In this study, L-CHAP@PLA facilitated macrophage efferocytosis in the inflammation microenvironment. Subsequently, promoting M2 polarization and suppressing M1 polarization decreases the M1/M2 ratio, achieving the attenuation of the inflammatory response and modulating immune homeostasis. However, the response to tendon injury can be divided into three overlapping stages, namely the "inflammatory stage", the "proliferative or repair stage", and the "remodeling phase" [11]. This healing phase is characterized by profuse synthetic activity and is directed by macrophages and TDSCs. Therefore, further investigation is needed to understand the role of L-CHAP@PLA in modulating TDSCs homeostasis within the tendon injury microenvironment.

2.6. L-CHAP@PLA-mediated enhanced macrophages efferocytosis promoted TDSCs tenogenic differentiation

To explore the effect of L-CHAP@PLA modulated macrophages on regulating TDSCs homeostasis in the tendon injury microenvironment, we investigated the expression of tendon repair-related markers and inflammation signal pathways by IF and WB assays after stimulation of TDSCs with tenogenic differentiation medium following co-incubation with macrophages treated with L/D/Rac-CHAP@PLA. It is known that Mohawk (MKX) and Scleraxis (SCX) are recognized as tenogenic transcription factors pivotal for differentiation. Tenomodulin (TNMD) is a tendon-specific marker supporting TDSC self-renewal, and Type I collagen (COL1) is a principal constituent of the TDSC-secreted extracellular matrix [13]. As depicted in Fig. 6a–e, the IF assay showed that the MKX, SCX, TNMD, and COL1 expression levels were all significantly upregulated in TDSCs after co-incubation with macrophages treated with L-CHAP@PLA compared to the control group and IL-1β group, which may contribute to improved tendon repair. Moreover, the WB results also indicated that the expression levels of tendon repair-related markers including SCX, TNMD, MKX, and COL1 in TDSCs in the L-CHAP@PLA group were the highest among all the groups, which was similar to that of the IF results, further demonstrating the role of L-CHAP@PLA in promoting the tenogenic differentiation of TDSCs in vitro (Fig. S6, Supporting Information). Furthermore, the NF-κB and IL-17 pathways were found to be notably suppressed in TDSCs in the L-CHAP@PLA group compared to both the control group and IL-1β group, as evidenced by WB assay (Fig. 6g–h). These results suggested that L-CHAP@PLA modulated macrophage efferocytosis could attenuate inflammation injury of TDSCs by downregulating the IL-17-NF-κB pathways, and then promote TDSCs tenogenic differentiation. Our investigation into the impact of L-chiral hydroxyapatite on macrophage immune homeostasis and TDSCs homeostatic modulation in vitro yielded encouraging results. Thus, we believe that L-chiral hydroxyapatite is a suitable choice for fabricating chiral coating for tendon repair.

2.7. L-CHAP@PLA effectively promoted tendon repair in vivo

To further ascertain the in vivo efficacy of L-CHAP@PLA in promoting regenerative tendon repair, an Achilles tendon injury model in rat was established as previously reported [43]. As shown in Fig. 7a, tendons in the control group formed granulation tissue at 1 and 4 weeks after surgery at the macroscopic level, accompanied by an intense inflammatory response. In contrast, the L-CHAP@PLA group exhibited much milder edema. At 8 weeks postoperatively, the L-CHAP@PLA group showed a denser appearance near the native tendon, while the control group displayed coarse and tough scar tissue at the repair site. At the histological level (Fig. 7b), H&E staining revealed increased disruption of matrix alignment and infiltration of inflammatory cells in the control group. Conversely, the L-CHAP@PLA group had more regular matrix alignment with fewer inflammatory cells and vessels. Alcian blue staining revealed that collagen fibers in the control and D-CHAP@PLA groups appeared more disorganized and loose at 1 and 4-weeks post-surgery compared to those in the L-CHAP@PLA and Rac-CHAP@PLA groups. Following an 8-week interval after surgery, the control group and D-CHAP@PLA group exhibited strongly positive Alcian blue staining, suggesting the formation of fibrocartilaginous tissue. While the tendons in the L-CHAP@PLA group exhibited a notably organized configuration at 1 and 4 weeks after surgery, and the density of collagen fiber increased significantly at 8 weeks. Furthermore, the semi-quantitative Bonar histological grading system was performed to evaluate tendon healing (Fig. 7c) [44]. The histological Bonar scores for the L-CHAP@PLA group were significantly lower at 1, 4, and 8 weeks compared to the control and D-CHAP@PLA groups, suggesting enhanced tendon healing in rats treated with L-CHAP@PLA. Immunohistochemical results showed that tendon-specific transcription factors MKX and SCX, and Proliferating cell nuclear antigen (PCNA) were
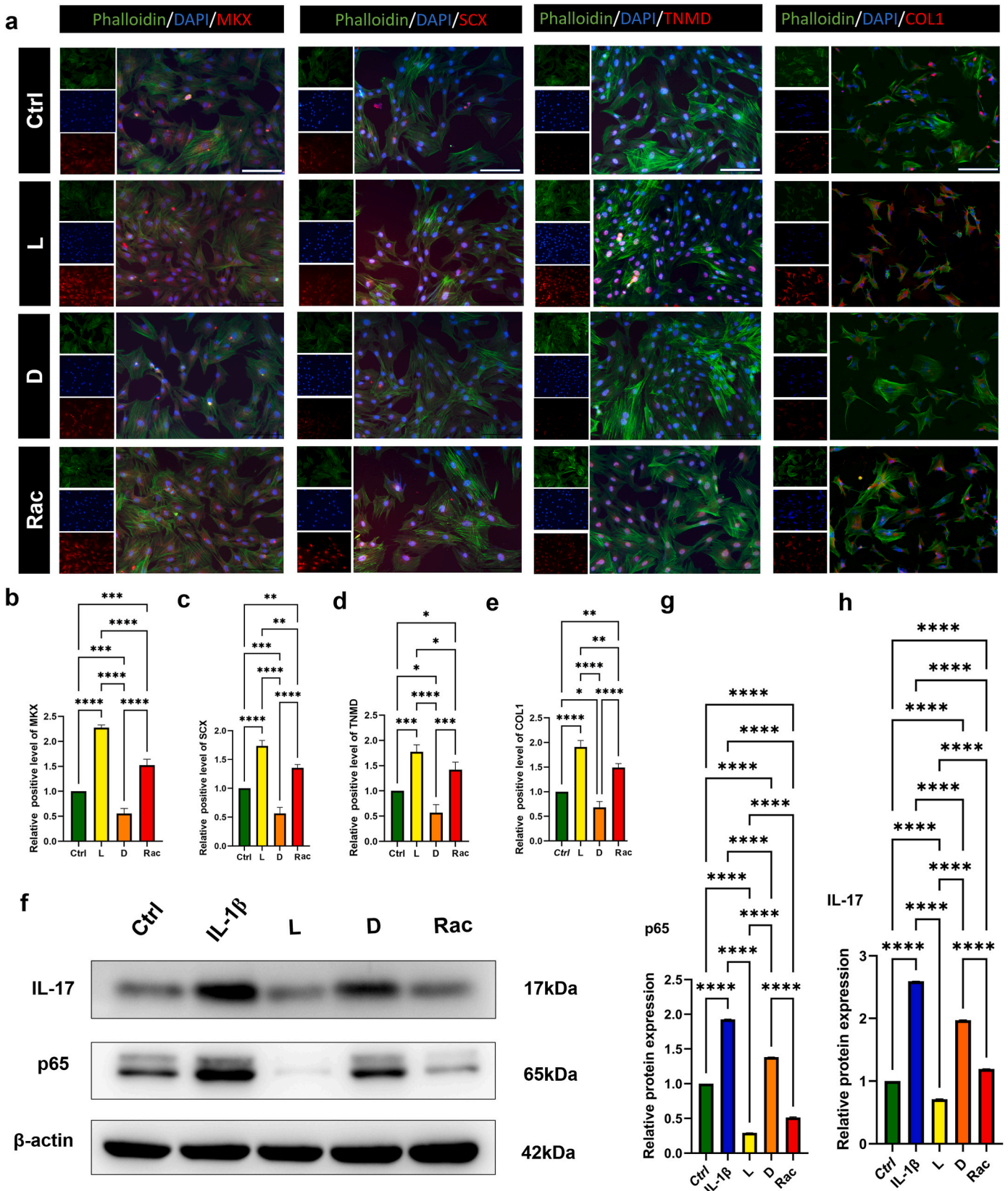
Fig. 6. The pro-efferocytosis effect of L-CHAP@PLA promoted TDSCs tenogenic differentiation. a) Representative fluorescence staining images of MKX, SCX, TNMD, and COL1 in TDSCs after co-incubation with each group. scale bar: 100 μm. Assessment of the relative fluorescent level of b) MKX, c) SCX, d) TNMD, and e) COL1. f) Western blot analysis of IL-17 and NF-κB p65 signalling pathway-related proteins in TDSCs (n = 5). Corresponding relative protein quantification, including g) IL-17 and h) p65. *p < 0.05, **p < 0.01, ***p < 0.001, ****p < 0.0001, indicates significant differences between the two groups.
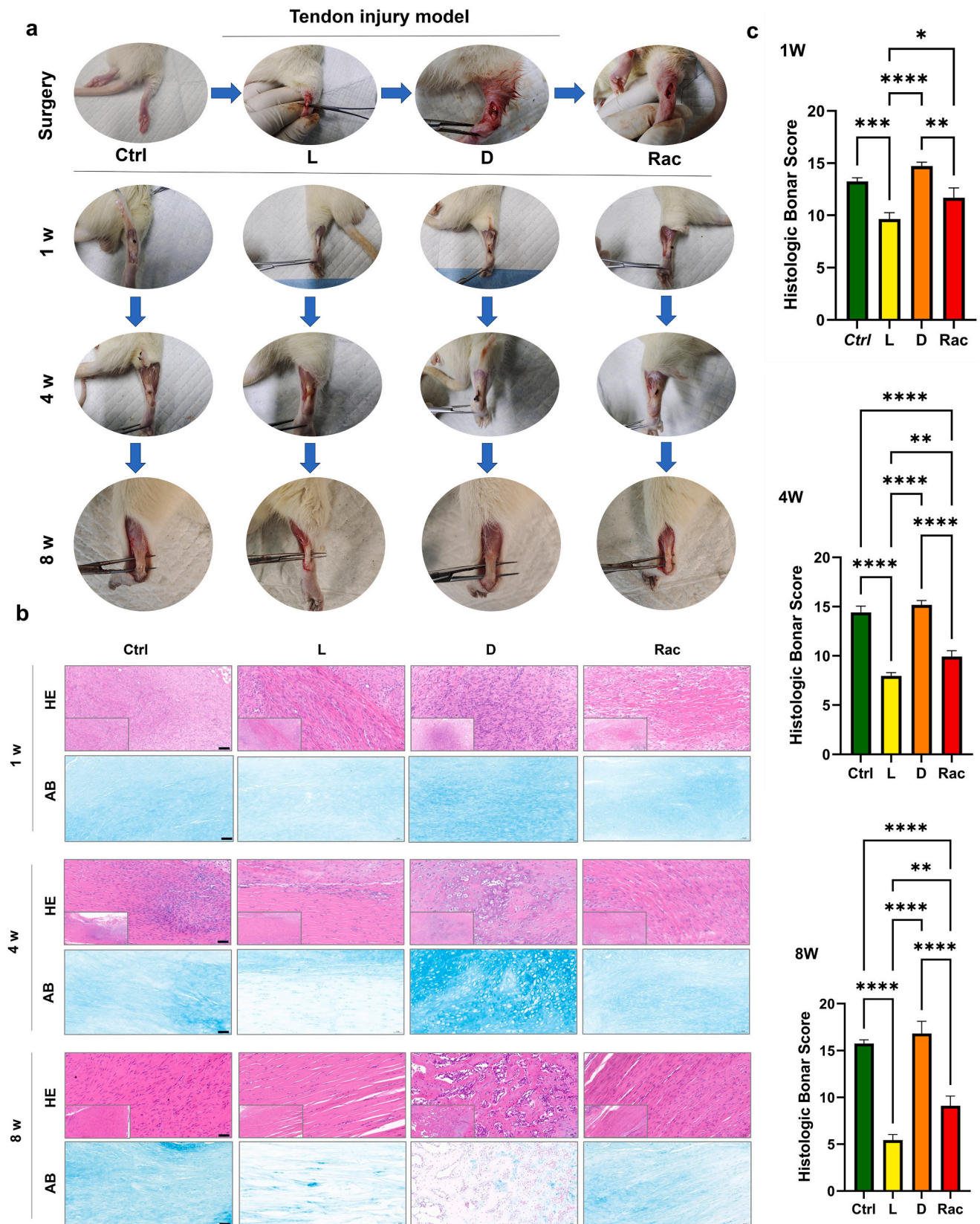
Fig. 7. L-CHAP@PLA promoted structural repair of injured tendons at macroscopic and histological levels in vivo. a) Schematic diagram of the surgical process of the tendon injury rat model, and gross view of injured tendons from control, L-CHAP@PLA, D-CHAP@PLA, and Rac-CHAP@PLA groups at various time points postinjury (n = 5). b) Representative images of H&E staining and Alcian blue staining of tendons from different groups at 1, 4, and 8 weeks postinjury, scale bar: 50 μm. c) Semiquantitative Bonar scores for histological analysis of different groups at various time points postinjury. *p < 0.05, **p < 0.01, ***p < 0.001, ****p < 0.0001, indicates significant differences between the two groups.

significantly upregulated in the L-CHAP@PLA group in the early stage of tendon healing, indicating enhanced initiation of tenogenesis (Fig. 8a–b). During the middle and advanced stages of tendon healing, the L-CHAP@PLA group exhibited increased expression of MKX, SCX, TNMD, and COL I, reflecting more mature tendon-specific ECM yield after L-CHAP@PLA treatment (Fig. 8c–f). It is worth noting that Rac-CHAP@PLA could also enhance the expression of tendon-specific markers after surgery. This effect may be attributed to R-CHAP containing certain L-chiral structure hydroxyapatite components.

To further evaluate the functional performance of rats after tendon injury, gait analysis was conducted using the Visual Gait analysis system (Xinruan, Shanghai). Gait parameters of rats 8 weeks after surgery, such as footprints and relative pressure difference of footsteps were assessed using the computer vision processing software provided by the analysis system (Fig. 9a). The results showed rats treated with L-CHAP@PLA had wider and shorter footprints and smaller pressure differences between left and right hind feet compared to the control group, D-CHAP@PLA group, and Rac-CHAP@PLA group, suggesting better motor function and recovery. At the ultrastructural level, transmission electron microscopy (TEM) was used to assess the alignment, density, and diameters of collagen fibers, which are important predictors of the mechanical properties of tendon healing. We found higher fibril density and larger fibril diameters in the L-CHAP@PLA group (Fig. 9b), which was confirmed by further statistical analysis of collagen fibril diameters (Fig. 9c–f), indicating enhanced tendon recovery. As the tissues transmit forces, when evaluating tendon structure, it's also crucial to consider the biomechanical properties. The Instron universal testing system was used to analyze tendons' biomechanical properties (stiffness, failure force, modulus, and stress at failure) at 8 weeks postoperatively. The L-CHAP@PLA group exhibited a mean stiffness of 53.07 N mm^{-1}, which was greater than the values observed in the control group (28.40 N mm^{-1}), the D-CHAP@PLA group (25.47 N mm^{-1}), and the Rac-CHAP@PLA group (36.73 N mm^{-1}) (Fig. 9g). In the L-CHAP@PLA group, the failure force was greater at 93.57 N compared to the control group at 58.90 N (Fig. 9h). The mean tensile modulus of the L-CHAP@PLA group (73.33 MPa) was significantly higher than that of the other groups (24.67 MPa in the control group, 26.87 MPa in the D-CHAP@PLA group, and 51.83 MPa in the Rac-CHAP@PLA group) (Fig. 9i). The L-CHAP@PLA group exhibited a stress at failure of 16.73 MPa, significantly surpassing the values of the other groups (5.40 MPa in the control group, 6.00 MPa in the D-CHAP@PLA group, and 12.53 MPa in the Rac-CHAP@PLA group) (Fig. 9j). In general, L-CHAP@PLA effectively promoted tendon repair in vivo.

2.8. Promotion of tendon healing with L-CHAP@PLA via macrophages efferocytosis-modulated M1/M2 polarization

To further elucidate the specific mechanism by which L-CHAP@PLA promoted tendon repair in vivo, we investigated it based on the rat Achilles tendon injury model. The Achilles tendon of rats on days 3 and 7 after L-CHAP@PLA intervention was harvested and subjected to immunofluorescence staining analysis. Fig. 10a–c demonstrates a significant reduction in macrophage infiltrates in the Achilles tendon cross-sectional IF staining of rats on day 3 following L-CHAP@PLA treatment. Additionally, there was a notable upregulation of the M2 marker Arg-1 expression compared to the control and D-CHAP@PLA groups. On day 7 after L-CHAP@PLA intervention, the expression of M1 marker i-NOS was significantly downregulated compared to the control and D-CHAP@PLA groups, and macrophages with M2 phenotype predominated in the L-CHAP@PLA group (Fig. 10d–f), which favored promoting inflammation regression, tenocyte proliferation, and ECM deposition. Moreover, the expression level of macrophage efferocytosis markers including GAS6, MerTk, MFGE-8, CX3CR1, and CD36 in the L-CHAP@PLA group at 3 days after surgery were higher than those in the other groups (Fig. 11a–f). Enhanced macrophage efferocytosis mediated by L-CHAP@PLA was further amplified on day 7 after surgery

(Fig. 11g–l), suggesting that L-CHAP@PLA can promote macrophage efferocytosis action by modulating macrophage polarization. Overall, these findings confirm that L-CHAP@PLA promotes tendon healing through a macrophage-homeostatic modulation strategy in vivo.

2.9. Biocompatibility evaluation for the L-CHAP@PLA in vivo

For implantable materials, the evaluation of in vivo biocompatibility is indispensable. The in vivo study verified satisfactory biocompatibility of different CHAP@PLA membranes in vivo. After an 8-week implantation of different CHAP@PLA membranes, H&E staining was performed to assess the morphology of major organs including the heart, liver, spleen, lung, and kidney in rats. The H&E staining results exhibited no structural abnormality among all groups (Fig. 12a). Besides, detecting serum biochemical index also serves as an effective method for evaluating the biosafety of biomaterials. Eight weeks after surgery, blood was drawn from the rats' caudal vein to evaluate liver and kidney function. Serum biochemical indices, including albumin (ALB), alanine aminotransferase (ALT), aspartate transaminase (AST), blood urea nitrogen (BUN), and creatinine (CREA), were evaluated, revealing no significant differences across all groups (Fig. 12b). PLA has good biodegradability and biocompatibility, and is suitable for tissue repair [45]. Hydroxyapatite is initially recognized for its exceptional biocompatibility and bioactivity and can be degraded into inorganic salts in vivo [46]. The L-CHAP@PLA is formulated from these two components and naturally exhibits satisfactory biocompatibility.

Some limitations are involved in our study. Firstly, we only selected the classic rat tendon injury model to investigate the effect of chiral hydroxyapatites on tendon healing, multiple animal models and larger animal models should be considered in future studies, such as rabbit or monkey. Secondly, since the short-term nature of the tendon injury animal model limited our observation of the changes in long-term physiological processes, long-term animal tracking experiments can de designed in further studies. Finally, there are still huge challenges in translating our study into the treatment of human tendon injury in the future due to the differences in physiological structures and functions between humans and animals, the complexity of the manifestations and internal mechanisms of diseases among different species, as well as ethical and regulatory constraints.

3. Conclusions

In this study, we initially deposited PLA electrospun membranes using traditional electrospinning. Subsequently, chiral hierarchical structure hydroxyapatite nanoplates were coated on a PLA electrospinning membrane by a facile chiral malic acid molecules-induced self-assembly strategy. L-chiral hydroxyapatite exhibited superior bioactivity and biocompatibility compared to the D-chiral and Rac-chiral hydroxyapatite. It was verified that L-CHAP@PLA promoted tendon repair by enhancing macrophage efferocytosis and M2 polarization through downregulated IL-17-NF-κB signaling, thereby promoting cell proliferation and tenogenic differentiation of TDSCs. Based on our findings, we believe that L-chiral hydroxyapatite nanoplates coated on PLA electrospun membrane represent a simple and effective treatment for promoting tendon regeneration and hold tremendous prospects for application in clinical practice.

4. Materials and methods

4.1. Materials

PLA substrate was obtained from DHU (Donghua University). Sodium chloride (NaCl, 99.5 %), sodium bicarbonate (NaHCO$_3$, 99.8 %), potassium chloride (KCl, 90 %), dipotassium phosphate (K$_2$HPO$_4$), magnesium chloride hexahydrate (MgCl$_2$.6H$_2$O, 99.5 %), sodium sulfate (Na$_2$SO$_4$, 98 %), calcium chloride (CaCl$_2$, 99.8 %) were obtained from
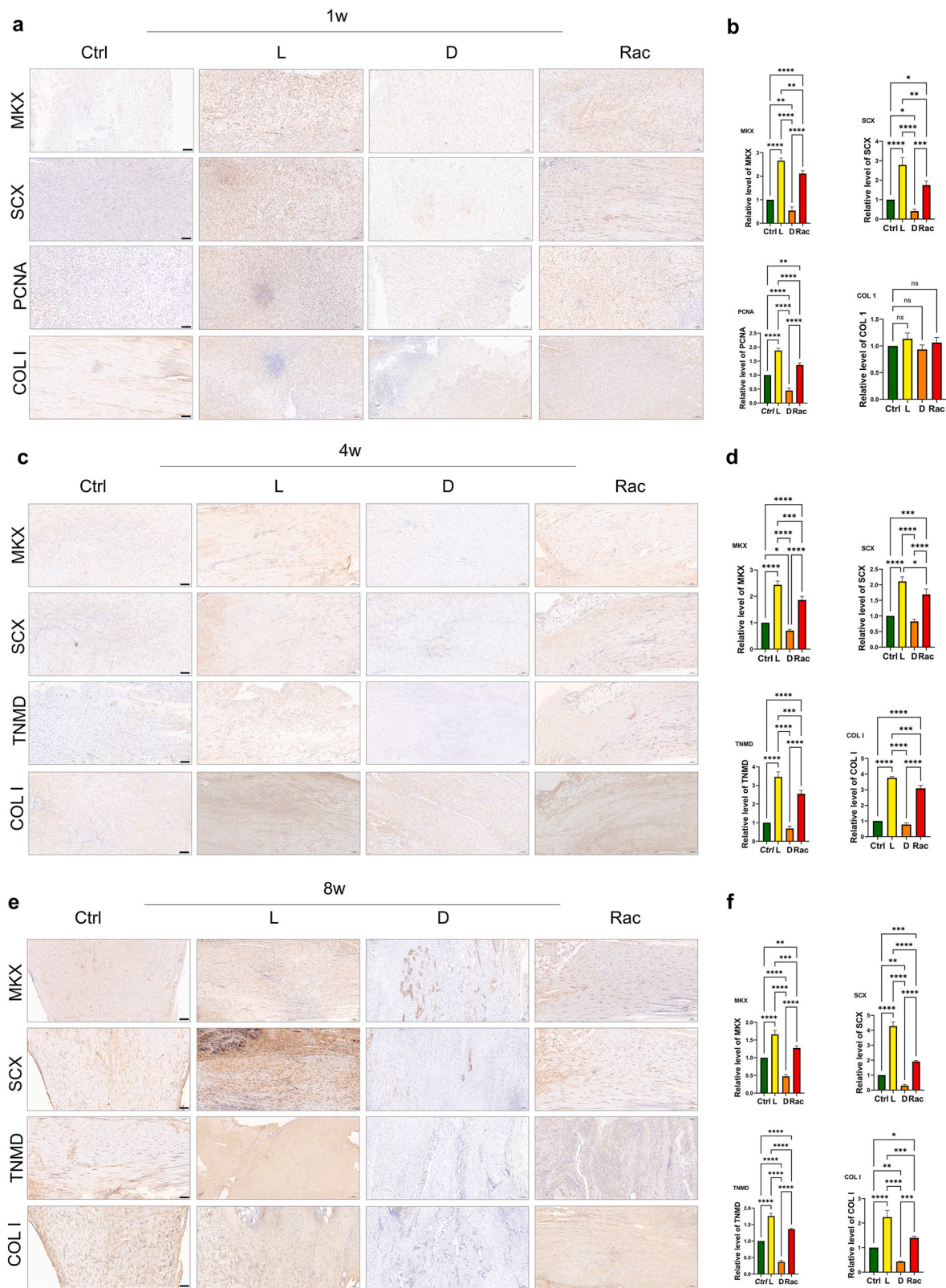
Fig. 8. L-CHAP@PLA promoted structural repair of injured tendons at macroscopic and histological levels in vivo. a) Representative images of immunohistochemical staining of tendon markers (MKX, SCX, PCNA, COL1) in early stage, and b) corresponding semiquantitative analysis of expression level of tendon marker (n = 5). c) Representative images of immunohistochemical staining of tendon markers (MKX, SCX, TNMD, COL1) in mid-stage, and d) corresponding semiquantitative analysis of expression level of tendon marker (n = 5). e) Representative images of immunohistochemical staining of tendon markers (MKX, SCX, TNMD, COL1) in advanced stage, and f) corresponding semiquantitative analysis of expression level of tendon marker (n = 5). scale bar: 100 μm ns means not significant, *p < 0.05, **p < 0.01, ***p < 0.001, ****p < 0.0001, indicates significant differences between the two groups.
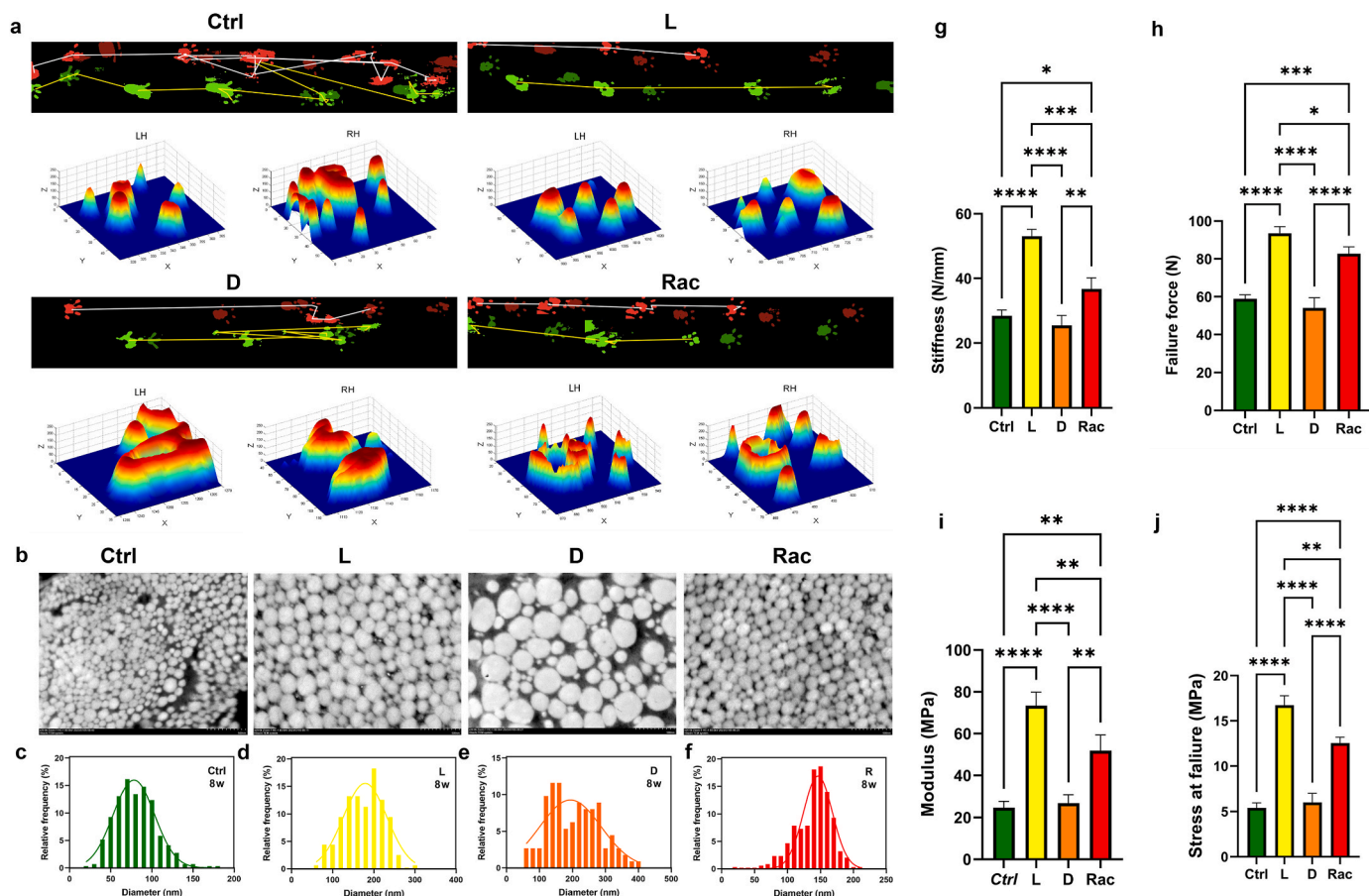
Fig. 9. L-CHAP@PLA improved ultrastructural morphology and promoted functional repair of injured tendons at various time points postinjury. a) Representative rat footprint images and relative pressure difference analysis of footsteps from control, L-CHAP@PLA, D-CHAP@PLA, and Rac-CHAP@PLA groups. b) Representative TEM images of repaired tendons, scale bar: 500 nm. c-f) Representative analysis of the distribution of collagen fibril diameter in the control, L-CHAP@PLA, D-CHAP@PLA and Rac-CHAP@PLA groups. The mechanical characteristics of injured tendons were assessed, including g) stiffness, h) failure force, i) modulus, and j) stress at failure. *$p < 0.05$, **$p < 0.01$, ***$p < 0.001$, ****$p < 0.0001$, indicates significant differences between the two groups.

Sinopharm Chemical Reagent. D-, L- and Racemic-malic acid were purchased from Tansoole. Hydrochloric acid (99.9 %), amino acids, and Tris(hydroxymethyl)aminoethane (CAS:77-86-1, 99.8 %) were purchased from J & K Chemical Technology.

4.2. Substrate treatment

The PLA substrate is immersed in a substantial amount of deionized water. Subsequently, it is alternately washed three times with ethanol under ultrasonic conditions and then washed with water. Finally, it is soaked in 0.1M calcium chloride solution 30 min.

4.3. Preparation of CHAP@PLA

The preparation of CHAP@PLA with a well-defined chiral structure was achieved through the previously reported methods for synthesizing chiral inorganic materials. Briefly, 0.2 mmol malic acid is dissolved in 20 mL SBF solution and stirred well to ensure complete dissolution. Then, processed PLA substrate was added to the mixed solution, and the PLA substrate was completely immersed in the solution. After that, cover the beaker mouth with plastic wrap, place the beaker in a 37°C-water bath, and allow mineralization to stew for 24 h. After the reaction, the PLA membrane was removed. CHAP@PLA was obtained by alternating cleaning with anhydrous ethanol and deionized water three times, and then freeze-drying.

4.4. Circular dichroism spectrometer

DRCD and UV/Vis spectra were observed through a spectropolarimeter (JASCO J-1500) equipped with a DRCD device. The membranes were positioned between the incident light in a normal direction and a black backboard. The integrating sphere collected all the reflected light before it reached the CD detector.

4.5. Fourier transform infrared spectrometer (FTIR)

FTIR patterns were recorded on a Thermelfeld iD1, Near-infrared spectrometer for solid measurement, operating temperature 5°C–40 °C; The working relative humidity of the instrument is 5%–95 %; Power consumption is less than 100VA.

4.6. Mechanical property test (MhP)

MhP was obtained using a TH-8100ST tensile and torsion composite testing machine (TopHung Machine Equipment Co.Ltd). Detailed steps are as follows: 1. Start the main power switch to make the power supply pass through each control panel of the machine; 2. The correct device test piece, select the fixture according to the type of test material, the test piece is first clamped on the upper fixture, start the motor to lift the upper and lower fixture of the moving plate to the appropriate position to clamp the test piece, the test piece cannot be held by tension or pressure, so as not to affect the test result:3. Before the test, adjust the upper and lower stroke setting rings to the upper and lower limits of the
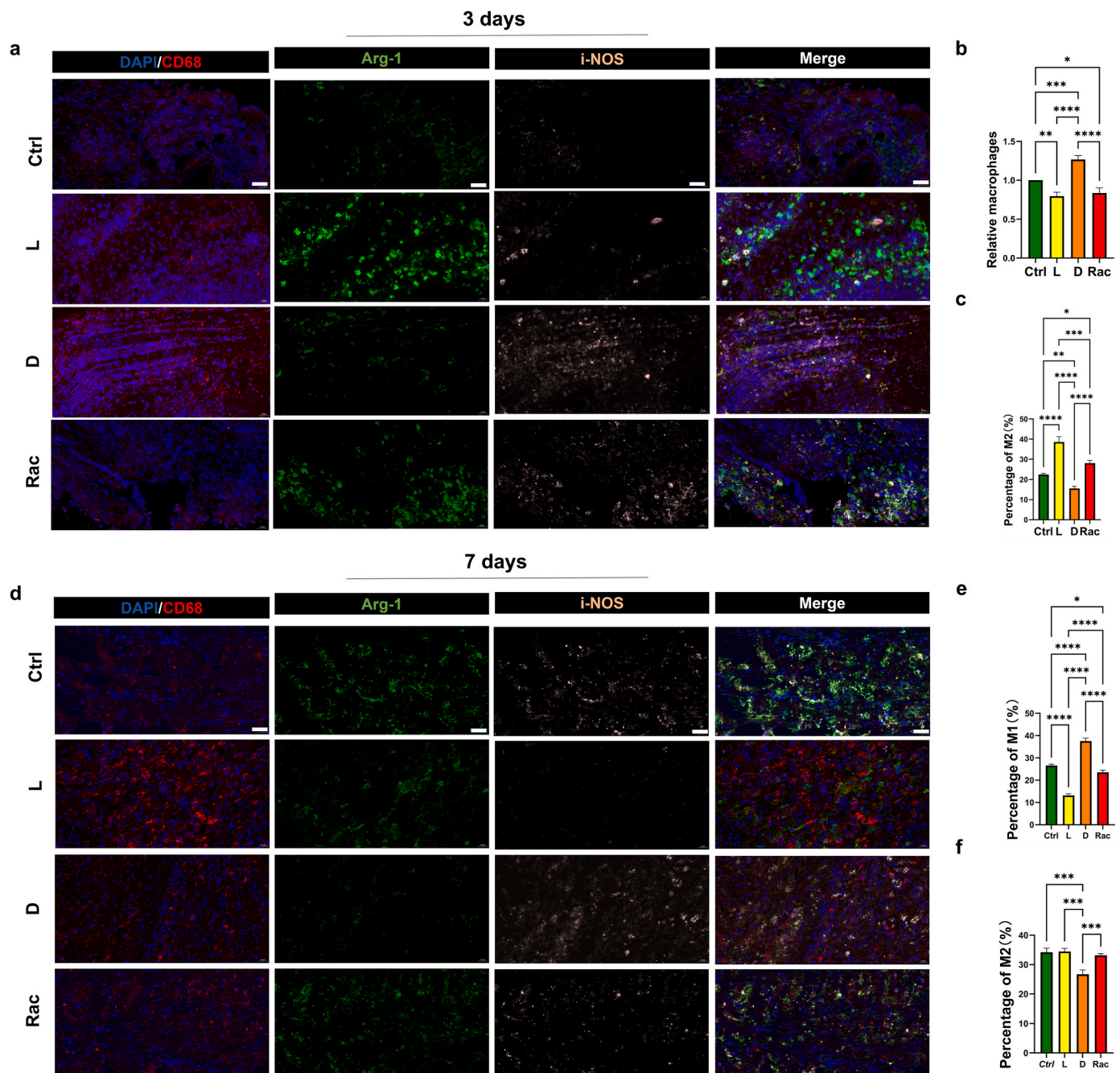
Fig. 10. L-CHAP@PLA promoted M2 phenotype polarization of macrophages and reduced inflammation damage. a) Representative images of triple immunofluorescence staining for CD68 (red), Arg-1(green), and i-NOS (pink) in the injury tendon at 3 days after surgery (n = 5). Scale bar, 20 μm. Corresponding semiquantitative analysis of b) number of macrophages and c) proportion of M2 polarization. d) Representative images of triple immunofluorescence staining for CD68 (red), Arg-1(green), and i-NOS (pink) in the injury tendon at 7 days after surgery. Scale bar, 20 μm. Corresponding semiquantitative analysis of e) percentage of M1 and f) percentage of M2. *p < 0.05, **p < 0.01, ***p < 0.001, ****p < 0.0001, indicates significant differences between the two groups.

required range, so that the lower fixture is behind this range will touch the limit switch and stop; 4. Select the appropriate test speed, and turn the speed knob on the control panel to the speed indicator number that has been determined: 5. Start the test software, and zero the data, ready to accept the test; 6. Start the motor to make the moving plate rise or fall to start the test, at which time the tensile value of the specimen is displayed, until the specimen breaks, the load remains the maximum value, after recording the value, remove the fractured specimen, and then clamp the specimen in accordance with the above method and the test software value gauge zero before testing. If the test has been completed, please turn off the power supply.

4.7. Contact angle (CA)

CA was obtained utilizing a contact angle meter (SINDIN Dongguan Sheng Ding Precision Instrument Co., LTD). Detailed steps are as follows: Fix the solid/membrane sample to the test plate; Choose an appropriate liquid and fill a syringe with it. Carefully manipulate the valve to extrude a droplet, which should hover above the sample surface without contacting it. Activate the camera system to focus on the droplet, and capture an image along the droplet's line of contact with the sample.
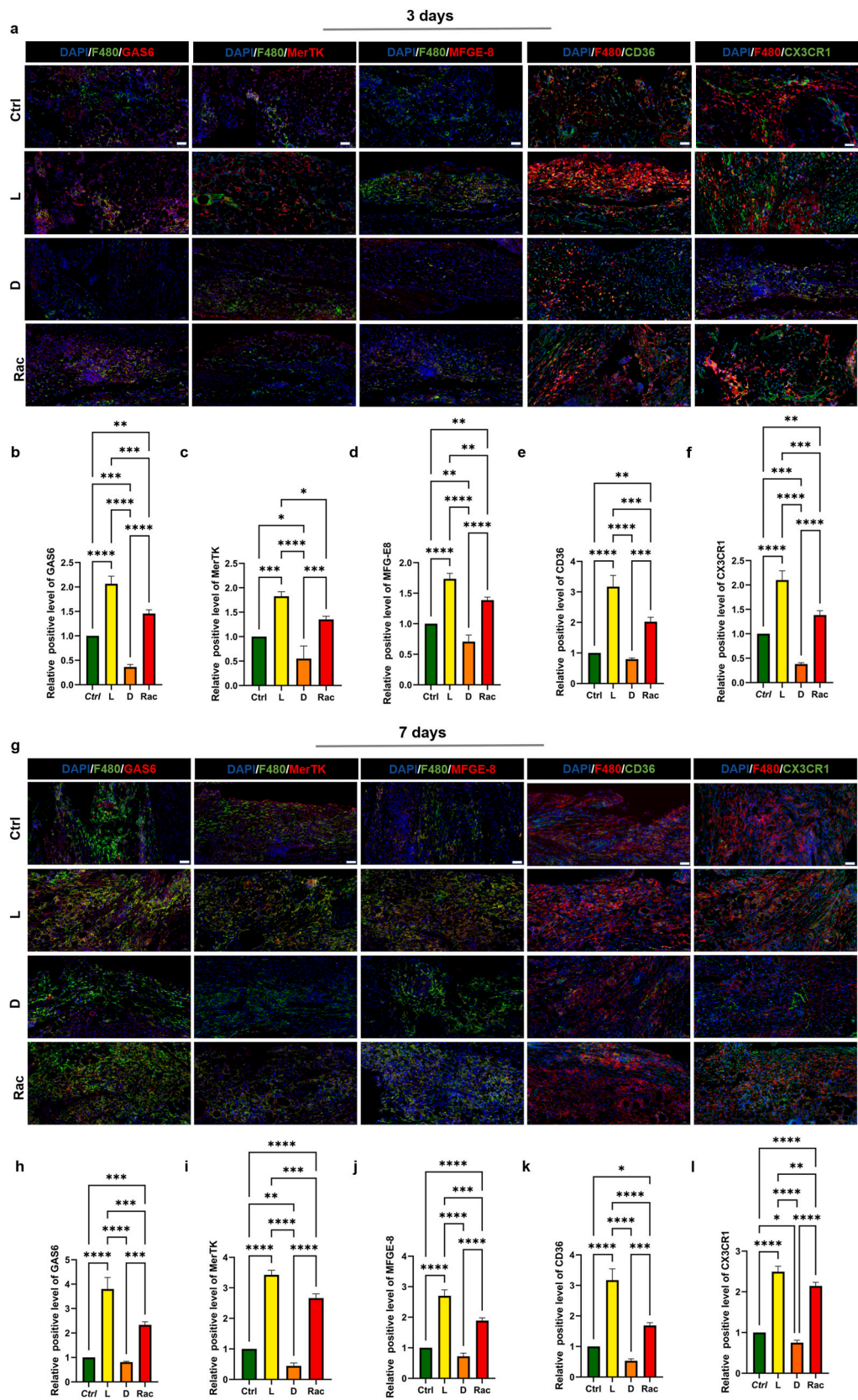
Fig. 11. L-CHAP@PLA enhanced efferocytosis and regulated the immune function of macrophages. a) Representative images of double immunofluorescence staining for markers related to macrophage efferocytosis effect in the injury tendon 3 days after surgery (n = 5). Scale bar, 20 μm. Semiquantitative analysis of relative positive level of b) GAS6, c) MerTK, d) MFG-E8, e) CD36, and f) CX3CR1. g) Representative images of double immunofluorescence staining for markers related to macrophage efferocytosis effect in the injury tendon 7 days after surgery. Scale bar, 20 μm. Semiquantitative analysis of relative positive level of h) GAS6, i) MerTK, j) MFG-E8, k) CD36, and l) CX3CR1. *p < 0.05, **p < 0.01, ***p < 0.001, ****p < 0.0001, indicates significant differences between the two groups.
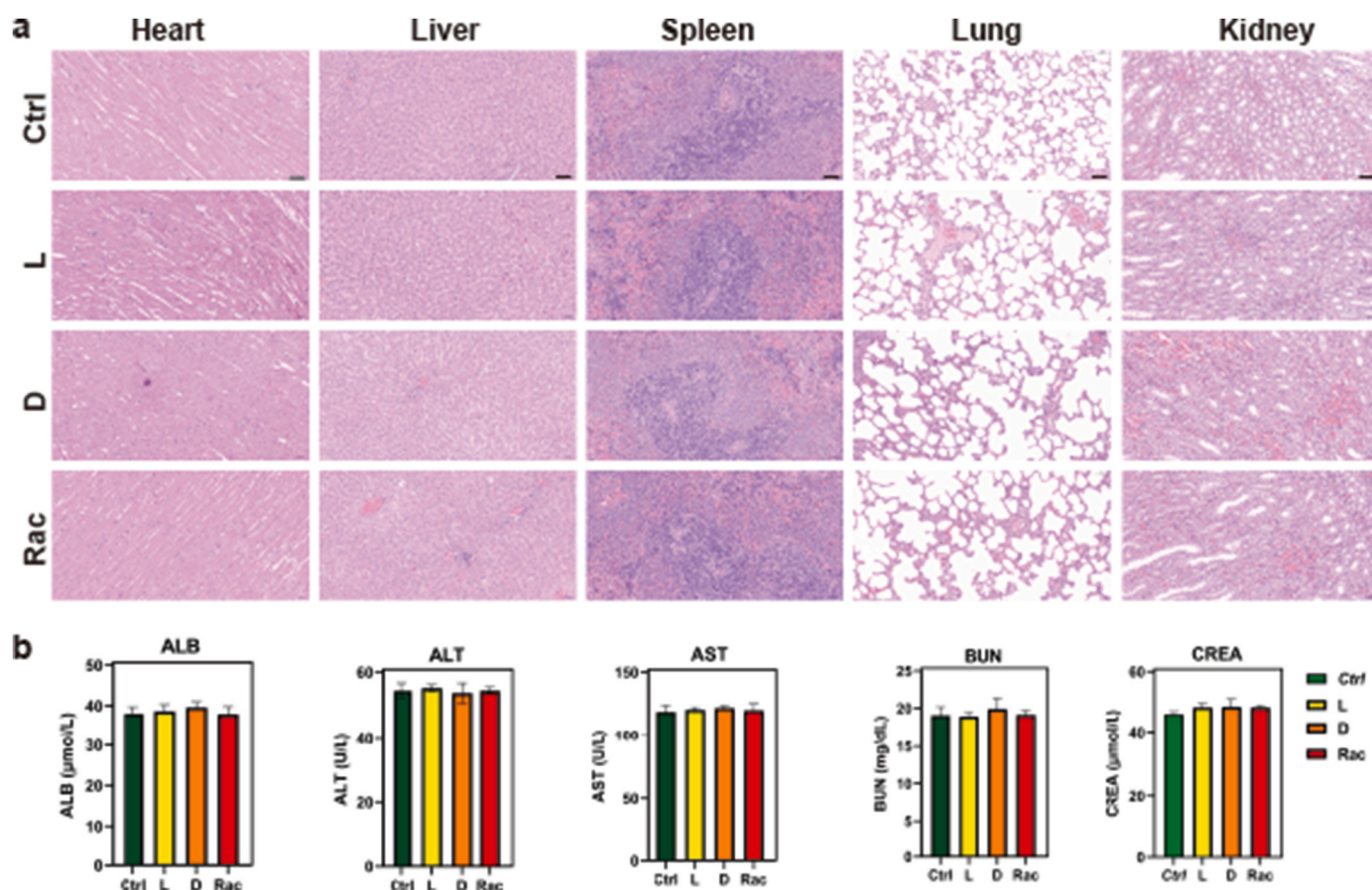
Fig. 12. Verification of the in vivo biological safety of CHAP@PLA. a) Morphology of the major function organ (heart, liver, spleen, lung, and kidney) from control, L-CHAP@PLA, D-CHAP@PLA, and Rac-CHAP@PLA groups at 8 weeks postoperatively (n = 5), scale bar: 50 μm. b) Blood biochemistry tests at 8 weeks postoperatively (n = 5). ALB, albumin; ALT, alanine aminotransferase; AST, aspartate transaminase; BUN, blood urea nitrogen; CREA, creatine. No significant differences between the two groups.

4.8. Cell culture

In this study, the isolations of TDSCs and macrophages were performed following the established methods [47,48]. To isolate TDSCs, the obtained Achilles tendon from male C57BL/6 mice was cut into small pieces and digested with collagenase I and dispase within a shaking incubator preheated to 37 °C for 2 h. After digestion, the mixture was subjected to filtration and centrifugation processes. Subsequently, the successfully extracted cells were cultured and passaged using a α-MEM (Gibco) medium for further experiments. For the isolation of BMDMs, the first step was to excise the tibia, and then flush the bone marrow out to the culture plate with PBS. The erythrocytes lysis buffer (Service, China) was used to remove the erythrocytes of bone marrows, and the bone marrows were cultured in complete RPMI 1640 medium supplement with M-CSF (40 ng/mL, Peprotech, China) for three days. Subsequently, the suspended cells in the medium were removed, and the medium was renewed for an additional three-day incubation. After the confluence rate reached 90 %, the BMDMs were harvested with a cell scraper for further use.

4.9. Biocompatibility assay in vitro

The viability and cell proliferation of BMDMs and TDSCs were evaluated utilizing a suite of methodologies, including the CCK-8, EdU incorporation, live-dead staining, and flow cytometry analysis.

In the execution of the CCK-8 assay, the BMDMs and TDSCs were cultured into the lower chamber of 24-well plates (20000 cells/well; five replicates per group). After cell adhesion, the CHAP@PLA membrane

was placed in the upper chamber. BMDMs were incubated for one day, while TDSCs were incubated for one, three, and five days. Then the cells were added to CCK-8 reagent and maintained under incubation at a temperature of 37 °C for another 2 h. Subsequently, the optical density of the culture solution in each well was quantified utilizing a microplate reader (Thermo, USA) at 450 nm.

The proliferation rate of TDSCs was also evaluated using the EdU proliferation kit (Beyotime, China). Firstly, TDSCs were incubated in 24-well plates (20000 cells/well) coated with L-CHAP, D-CHAP, or R-CHAP membrane for 24h. Afterward, cells were labeled with the EdU (10 μM in cell medium) and incubated for 3 h, and then combined with working solution following the detailed manufacturer's instructions. Finally, the cells were imaged using a Leica epifluorescence microscope (Leica, Germany), and the EdU-positive cells were counted by Image J Software (Image 1.53a, USA).

The live/dead staining was performed to evaluate the cytotoxicity of hydroxyapatite with different chiral structures. TDSCs were incubated on cell well plates treated with L-CHAP@PLA, D- CHAP@PLA, or Rac-CHAP@PLA membrane for 24 h. Subsequently, live/dead kit reagents (Beyotime, China) were added to each well plate for an additional 30 min incubation. The labeled cells were imaged using a Leica epifluorescence microscope, and counted by Image J Software.

4.10. Flow cytometry

After treatment with different CHAP membranes, the cells were combined with fluorescein-labeled primary antibodies on ice for 30 min. After centrifugation, the labeled cells were then subjected to a rinsing

process and reconstituted into a single-cell suspension. The specific fluorescence intensity of cells was determined by flow cytometry analysis. The data was finally subjected to comprehensive analysis utilizing Flowjo software for intricate examination and elucidation. Table S1 (Supporting Information) listed the detailed information on flow antibodies utilized in the present study.

4.11. Quantitative real-time PCR (qRT-PCR) analysis

RNA was extracted using an EZBioscience purification kit, following the manufacturer's protocol. Subsequently, complementary DNA synthesis was achieved utilizing the reverse transcription kit. Finally, SYBR Green qPCR Master Mix was utilized to quantify the expression levels of the target gene mRNA transcripts. The detailed information on the gene primers (Servicebio, Wuhan, China) utilized in the present study can be found in Table S2 (Supporting Information), and Glyceraldehyde-3-phosphate dehydrogenase (GAPDH) was employed as a reference gene for normalization purposes.

4.12. ELISA assay

Collect and centrifuge the cell culture medium to obtain the supernatant. The supernatant was then analyzed using the ELISA assay kit (Invitrogen, USA) to examine the expression levels of cytokines pertinent to macrophages, including IL-10, IL-6, IL-4, TNF-α, and TGF-β following the manufacturer's instructions.

4.13. Transcriptomic analysis

The total RNA extraction from macrophages was conducted utilizing the TRIzol reagent. RNA integrity was assessed subsequent to purification and amplification utilizing an Agilent 2100 Bioanalyzer. The VAHTS Universal V6 RNA-seq Library Prep Kit was subsequently employed for the construction of the RNA-seq libraries. Technical support for transcriptome sequencing and subsequent data interpretation was provided by OE Biotech, situated in Shanghai, China.

An Illumina Novaseq 6000 sequencing system was employed to sequence the constructed libraries, yielding 150 base pair paired-end reads. Fastp [49] was used to first process fastq format raw reads and remove the low-quality reads for the clean reads obtainment. The reference genome was mapped by the clean reads using HISAT [50]. The HTSeq-count [51] was utilized to compute the FPKM [52] values for each gene, thereby acquiring the corresponding read counts. Sample biological duplication was evaluated with PCA analysis conducted with R software version 3.2.0.

The DESeq2 [53] was utilized for the analysis of differential gene expression. To identify significantly differentially expressed genes (DEGs), a stringent threshold was applied, necessitating a Q-value below 0.05, accompanied by fold change values surpassing 1.5 for upregulated genes and dropping below 0.67 for downregulated genes. Hierarchical cluster analysis of differentially expressed genes (DEGs) was conducted using R (version 3.2.0) to elucidate the gene expression patterns across various groups and samples. Subsequently, significant enrichment terms were identified through WikiPathways enrichment, KEGG [54], GO [55] pathway analysis of DEGs, respectively. Meanwhile, Utilizing the GSEA software [56,57] for further signaling pathway analysis. A preselected gene collection was employed for the analytical procedure, following which the genes were hierarchically ordered according to the magnitude of their differential expression levels. Finally, A validation experiment was conducted to assess the prevalence of the predefined gene set in the upper and lower quartiles of the ranking list.

4.14. Western blot analysis

After washing with PBST three times, cell samples were lysed using the RIPA lysis buffer at 4 °C. Protein in the supernatant were isolated by subjecting the sample to centrifugation at a force of $10000 \times g$ for a duration of 20 min, while maintaining a temperature of 4 °C. Using the BCA protein kit (EpiZyme) for the quantification of protein concentration. Protein, each at a concentration of 20 μg, were subjected to SDS-PAGE utilizing EpiZyme gels within a Miniprotein III electrophoresis system (Bio-Rad, USA). Subsequently, the separated protein was transferred onto polyvinylidene fluoride (PVDF) membranes. Following blocking with a 5 % (w/v) solution of bovine serum albumin (BSA) or nonfat milk, the membranes were subjected to incubation with the primary antibodies at a temperature of 4 °C overnight. Subsequent to triple washing of the membranes with PBST solution, the membranes were incubated with goat anti-rabbit conjugated secondary antibodies, maintained at room temperature, for a duration of 1 h. The protein bands were visualized using the ChemiDoc CRS imaging system (Tanon, Beijing) for high-resolution analysis. The detailed information on Western blot antibodies can be found in Table S1 (Supporting Information).

4.15. Coculture assay

A porous membrane (Corning, USA) with a pore size of 0.4 μm was selected for the coculture assay. BMDMs treated with different CHAP/PLA membranes were cultured in the apical compartment, whereas TDSCs were cultured in the basal compartment with tenogenic differentiation medium.

4.16. Animal experiment

Male Sprague-Dawley rats, aged between eight to ten weeks, were maintained in a specific pathogen-free environment within the animal experimental facility at Shanghai Sixth People's Hospital. Male Sprague-Dawley rats at eight weeks of age were prospectively randomized into four experimental groups, each consisting of 20 rats. These groups were designated as follows: the control group (only accepting surgery without any further treatment); the L-CHAP@PLA group (L-CHAP@PLA membrane was used for wrapping the repaired Achilles tendons); the D-CHAP@PLA group (D-CHAP@PLA membrane was used for wrapping the repaired Achilles tendons); the Rac-CHAP@PLA group (Rac-CHAP@PLA membrane was used for wrapping the repaired Achilles tendons). Briefly, Rats were firstly anesthetized via intraperitoneal administration of a 0.6 % pentobarbital solution. After disinfecting and shaving the surrounding area of the calf, a precise skin incision was executed posteriorly on the calf using a sterile surgical blade to access the Achilles tendon. Subsequently, the Achilles tendon was transected transversely along the middle part. Subsequently, the Achilles tendon was sutured using the modified Kessler suture method. Before closing the skin incision, the repaired Achilles tendon was wrapped by a piece of CHAP@PLA membrane, while those only receiving surgery without membrane wrapping were taken as the control group. All rats were administered an intraperitoneal injection of meloxicam at a dose of 3 mg/kg following surgical procedures to mitigate postoperative pain. Rats were humanely euthanized at 3-day, 1-week, 4-week, and 8-week intervals post-surgery to obtain Achilles tendon samples for subsequent analytical procedures. All animals were maintained and handled with approval by the Institutional Review Board of Shanghai Sixth People's Hospital and strictly adhered to the ethical guidelines of The Basel Declaration (No.2024-09-LY-FCY-085).

4.17. Scanning electron microscopy and transmission electron microscopy

For scanning electron microscopy (SEM) analysis, tissue specimens measuring 1 × 1 mm were subjected to a double-fixation protocol, initially with a 2 % glutaraldehyde solution for a duration of 24 h, succeeded by fixation with 2 % osmium tetroxide for an additional 2 h. Following dehydration through a series of ethanol concentrations, the specimens underwent critical point drying and were subsequently

coated with gold via sputter-coating for a duration of 30 s. The Hitachi SU8020 model originating from Japan was employed to investigate the diameter and the spatial configuration of collagen fibers.

For transmission electron microscopy (TEM) analysis, the excised tissue samples were initially fixed with a 2.0 % solution of glutaraldehyde for a duration of 24 h, followed by postfixation with 2 % osmium tetroxide for an additional 2 h. Subsequently, the specimens were stained using a combination of lead citrate and uranyl acetate, prior to being embedded within an epoxy resin matrix for sectioning. Cross-sectional and sagittal slices were meticulously prepared utilizing an ultramicrotome (Leica, Germany). The ultrastructure of tendon was examined utilizing transmission electron microscopy (TEM), employing a Hitachi HT7700 model instrument manufactured in Japan.

4.18. Histological, immunohistochemical, and biocompatibility analyses

The Achilles tendon specimens from rats were harvested at weeks 1, 4, and 8 after surgery, and fixed overnight in 4 % paraformaldehyde. Following fixation, the harvested specimens were subjected to dehydration by immersion in a 30 % sucrose solution. Subsequently, the specimens were embedded within OCT (Thermo, USA), and longitudinally sectioned at approximately 10 μm intervals using a cryostat (Leica). Standard protocols were adhered to for the implementation of Alcian Blue and Hematoxylin and Eosin (H&E) staining to assess the change in tissue structure and composition.

Immunohistochemistry analysis was conducted to explore the protein expression level of tendon. Standard protocols were adhered to for the implementation of Alcian Blue and Hematoxylin and Eosin (H&E) staining techniques to assess the alterations in tissue structure and composition. Following this, the sections were further incubated with horseradish-peroxidase-conjugated secondary antibodies for 1 h. Immunohistochemistry sections were finally imaged using a Leica epifluorescence microscope (Leica, Germany).

To evaluate the biocompatibility of the materials in vivo, hematoxylin and eosin (H&E) staining was conducted on excised specimens of major functional organs, such as the liver, heart, spleen, lung, and kidney. Additionally, the caudal vein blood harvested from rats at 8 weeks postoperatively was used to evaluate liver and kidney function.

4.19. Immunofluorescence staining

Immunofluorescence analysis was also performed to explore the protein expression in macrophages in vivo. Following blocking with a 5 % bovine serum albumin solution for a duration of 1 h, the tissue sections were subjected to overnight incubation with primary antibodies targeting markers of macrophage polarization and efferocytosis at 4 °C. Subsequently, the sections were conjugated with fluorophore-labeled secondary antibodies under ambient temperature conditions. DAPI staining was employed to visualize the cellular nuclei. Immunofluorescence sections were finally imaged using a Leica epifluorescence microscope (Leica, Germany).

In vitro, BMDMs were treated with different CHAP@PLA membranes for 48 h. Following fixation with 4 % paraformaldehyde and subsequent permeabilization using 0.1 % Triton X-100, the subsequent procedures involved blocking with 5 % (w/v) BSA for 1 h, followed by an overnight incubation at 4 °C with a suite of primary antibodies, namely anti-F4/80, anti-CD206, anti-iNOS, anti-MerTK, and anti-MFGE-8. The specimens were then combined with fluorophore-conjugated secondary antibodies at ambient temperature before concluding with DAPI nuclear staining. Similarly, TDSCs cocultured with BMDMs were incubated with primary antibodies related to tendon impair including anti-COL-I, anti-TNMD, anti-MKX, and anti-SCX overnight at 4 °C, and further incubated with corresponding secondary antibodies, followed by DAPI staining. The detailed information on immunofluorescence staining antibodies can be found in Table S1 (Supporting Information).

4.20. Visual Gait analysis

Visual Gait analysis was conducted using the Visual Gait analysis system (Xinruan, Shanghai). During the experiment, the rats were placed on a walking platform that could record various walking parameters and were permitted to walk freely from one end of the platform to the other. A high-speed camera was used to record the rat's movement. Gait parameters such as footprints and relative pressure difference of footsteps were assessed using the computer vision processing software provided by the analysis system.

4.21. Mechanical testing

At 8-weeks post-surgery, the Achilles specimens were harvested and subjected to mechanical assessment utilizing an Instron tension/compression testing apparatus equipped with Fast-Track software (Model 5969, Massachusetts). The harvested Achilles tendon specimens were preserved at a subzero temperature of −80 °C. Subsequently, the specimens were gradually thawed at room temperature during the formal experiment, and the adjacent tissues were carefully excised. Subsequently, the samples were fixed to a custom fixture with high-strength thread. Following the application of an initial preload of 0.1 N, the specimens underwent cyclic elongation within the range of 0–0.5 mm at a constant rate of 5 mm/min, consisting of 20 consecutive cycles. Subsequently, the specimens underwent a load-to-failure assessment at a constant elongation rate of 5 mm per minute. The load-elongation characteristics of the composite material were meticulously documented, along with the associated failure modes. The primary structural performance metrics documented during the experimental procedure include stiffness, quantified in units of newtons per millimeter (N/mm); failure force, measured in newtons (N); the work exerted to failure, expressed in joules (J); stress relaxation, represented as a percentage (%); modulus of elasticity, delineated in megapascals (MPa); and the stress at failure, also specified in megapascals (MPa).

4.22. Statistical analysis

Data are presented as the mean ± standard deviation (SD). Data analysis was conducted utilizing GraphPad Prism 10 software (GraphPad Software, Inc., USA). Comparative analyses between the groups were conducted utilizing Student's t-test, while multiple comparisons were evaluated through one-way analysis of variance (ANOVA). To ascertain reproducibility, a minimum of three independent biological and technical replicates were conducted for each experimental trial. Statistical significance was determined at the threshold of $P < 0.05$.

Data and materials availability statement

All data underpinning the study's conclusions are presented in full within the manuscript.

CRediT authorship contribution statement

Gang Luo: Writing – original draft, Validation, Resources, Methodology, Investigation, Formal analysis, Data curation, Conceptualization. **Juehong Li:** Writing – original draft, Methodology, Investigation, Formal analysis. **Shuai Chen:** Resources, Methodology, Investigation, Data curation. **Zhengqiang Yuan:** Methodology, Investigation. **Ziyang Sun:** Investigation, Funding acquisition. **Tengfei Lou:** Methodology, Funding acquisition. **Zhenyu Chen:** Methodology, Investigation. **Hang Liu:** Methodology, Investigation. **Chao Zhou:** Writing – original draft, Supervision, Resources, Methodology, Investigation, Data curation, Conceptualization. **Cunyi Fan:** Writing – review & editing, Project administration, Methodology, Funding acquisition, Formal analysis, Data curation, Conceptualization. **Hongjiang Ruan:** Writing – review & editing, Supervision, Methodology, Investigation, Data curation,

Conceptualization.

Ethics approval and consent to participate

All the animal experiment protocols were approved by the Institutional Review Board of Shanghai Sixth People's Hospital and performed strictly adhered to ethical guidelines of The Basel Declaration (NO.2024-09-LY-FCY-085).

Funding

Declaration of competing interest

The authors declare that they have no conflict of interest

Appendix A. Supplementary data

Supplementary data to this article can be found online at https://doi.org/10.1016/j.bioactmat.2025.01.027.

References

[1] D. Docheva, S.A. Müller, M. Majewski, C.H. Evans, Biologics for tendon repair, Adv. Drug Deliv. Rev. 84 (2015) 222–239.

[2] M. Benjamin, E. Kaiser, S. Milz, Structure-function relationships in tendons: a review, J. Anat. 212 (3) (2008) 211–228.

[3] P. Sharma, N. Maffulli, Tendon injury and tendinopathy: healing and repair, J Bone Joint Surg Am 87 (1) (2005) 187–202.

[4] T. Nakajima, A. Nakahata, N. Yamada, K. Yoshizawa, T.M. Kato, M. Iwasaki, et al., Grafting of iPS cell-derived tenocytes promotes motor function recovery after Achilles tendon rupture, Nat. Commun. 12 (1) (2021) 5012.

[5] S. Thomopoulos, W.C. Parks, D.B. Rifkin, K.A. Derwin, Mechanisms of tendon injury and repair, J. Orthop. Res. 33 (6) (2015) 832–839.

[6] B.R. Freedman, A. Kuttler, N. Beckmann, S. Nam, D. Kent, M. Schuleit, et al., Enhanced tendon healing by a tough hydrogel with an adhesive side and high drug-loading capacity, Nat. Biomed. Eng. 6 (10) (2022) 1167–1179.

[7] N.L. Millar, K.G. Silbernagel, K. Thorborg, P.D. Kirwan, L.M. Galatz, G.D. Abrams, et al., Tendinopathy, Nat. Rev. Dis. Prim. 7 (1) (2021) 1.

[8] T.J. Koh, L.A. DiPietro, Inflammation and wound healing: the role of the macrophage, Expet Rev. Mol. Med. 13 (2011) e23.

[9] Y. Xiong, B.B. Mi, Z. Lin, Y.Q. Hu, L. Yu, K.K. Zha, et al., The role of the immune microenvironment in bone, cartilage, and soft tissue regeneration: from mechanism to therapeutic opportunity, Mil Med Res 9 (1) (2022) 65.

[10] Y. Xiong, B.B. Mi, M.A. Shahbazi, T. Xia, J. Xiao, Microenvironment-responsive nanomedicines: a promising direction for tissue regeneration, Mil Med Res 11 (1) (2024) 69.

[11] P.B. Voleti, M.R. Buckley, L.J. Soslowsky, Tendon healing: repair and regeneration, Annu. Rev. Biomed. Eng. 14 (2012) 47–71.

[12] D.M. Mosser, J.P. Edwards, Exploring the full spectrum of macrophage activation, Nat. Rev. Immunol. 8 (12) (2008) 958–969.

[13] J.Y. Sunwoo, C.D. Eliasberg, C.B. Carballo, S.A. Rodeo, The role of the macrophage in tendinopathy and tendon healing, J. Orthop. Res. 38 (8) (2020) 1666–1675.

[14] J. Lin, W. Zhou, S. Han, V. Bunpetch, K. Zhao, C. Liu, et al., Cell-material interactions in tendon tissue engineering, Acta Biomater. 70 (2018) 1–11.

[15] S. Wang, Z. Yao, X. Zhang, J. Li, C. Huang, Y. Ouyang, et al., Energy-supporting enzyme-mimic nanoscaffold facilitates tendon regeneration based on a mitochondrial protection and microenvironment remodeling strategy, Adv. Sci. 9 (31) (2022) e2202542.

[16] C. Cai, X. Zhang, Y. Li, X. Liu, S. Wang, M. Lu, et al., Self-healing hydrogel embodied with macrophage-regulation and responsive-gene-silencing properties for synergistic prevention of peritendinous adhesion, Adv. Mater. 34 (5) (2022) e2106564.

[17] Y. Xiong, B. Mi, G. Liu, Y. Zhao, Microenvironment-sensitive nanozymes for tissue regeneration, Biomaterials 309 (2024) 122585.

[18] S. Dutta, A.J. Gellman, Enantiomer surface chemistry: conglomerate versus racemate formation on surfaces, Chem. Soc. Rev. 46 (24) (2017) 7787–7839.

[19] X. Yao, Y. Hu, B. Cao, R. Peng, J. Ding, Effects of surface molecular chirality on adhesion and differentiation of stem cells, Biomaterials 34 (36) (2013) 9001–9009.

[20] X. Niu, R. Zhao, S. Yan, Z. Pang, H. Li, X. Yang, et al., Chiral materials: progress, applications, and prospects, Small 19 (38) (2023) e2303059.

[21] Z. Cai, C. Qu, W. Song, H. Wang, S. Chen, C. Zhou, et al., Hierarchical chiral calcium silicate hydrate films promote vascularization for tendon-to-bone healing, Adv. Mater. (2024) e2404842.

[22] H. Zhu, C. Xing, X. Dou, Y. Zhao, Y. Peng, C. Feng, et al., Chiral hydrogel accelerates Re-epithelization in chronic wounds via mechanoregulation, Adv. Healthcare Mater. 11 (21) (2022) e2201032.

[23] L. Xu, X. Wang, W. Wang, M. Sun, W.J. Choi, J.Y. Kim, et al., Enantiomer-dependent immunological response to chiral nanoparticles, Nature 601 (7893) (2022) 366–373.

[24] H. Yook, J. Hwang, W. Yeo, J. Bang, J. Kim, T.Y. Kim, et al., Design strategies for hydroxyapatite-based materials to enhance their catalytic performance and applicability, Adv. Mater. 35 (43) (2023) e2204938.

[25] X. Sun, Y. Gao, Z. Li, J. He, Y. Wu, Magnetic responsive hydroxyapatite scaffold modulated macrophage polarization through PPAR/JAK-STAT signaling and enhanced fatty acid metabolism, Biomaterials 295 (2023) 122051.

[26] H. Huang, W. Pan, Y. Wang, H.S. Kim, D. Shao, B. Huang, et al., Nanoparticulate cell-free DNA scavenger for treating inflammatory bone loss in periodontitis, Nat. Commun. 13 (1) (2022) 5925.

[27] M.S. Singhvi, S.S. Zinjarde, D.V. Gokhale, Polylactic acid: synthesis and biomedical applications, J. Appl. Microbiol. 127 (6) (2019) 1612–1626.

[28] X. Wang, B. Ding, B. Li, Biomimetic electrospun nanofibrous structures for tissue engineering, Mater. Today 16 (6) (2013) 229–241.

[29] C. Zhou, S.Y. Zhang, J. Ai, P. Li, Y.J. Zhao, B.J. Li, et al., Enantioselective interaction between cells and chiral hydroxyapatite films, Chem. Mater. 34 (1) (2022) 53–62.

[30] Y. Wang, S. Jin, D. Luo, D. He, C. Shi, L. Zhu, et al., Functional regeneration and repair of tendons using biomimetic scaffolds loaded with recombinant periostin, Nat. Commun. 12 (1) (2021) 1293.

[31] L. Dong, J. Gong, Y. Wang, J. He, D. You, Y. Zhou, et al., Chiral geometry regulates stem cell fate and activity, Biomaterials 222 (2019) 119456.

[32] G.F. Liu, L.Y. Zhu, W. Ji, C.L. Feng, Z.X. Wei, Inversion of the supramolecular chirality of nanofibrous structures through Co-assembly with achiral molecules, Angew Chem. Int. Ed. Engl. 55 (7) (2016) 2411–2415.

[33] N. Sun, X. Dou, Z. Tang, D. Zhang, N. Ni, J. Wang, et al., Bio-inspired chiral self-assemblies promoted neuronal differentiation of retinal progenitor cells through activation of metabolic pathway, Bioact. Mater. 6 (4) (2021) 990–997.

[34] M. Sun, S.Q. Peng, C.L. Zhao, J.X. Huang, J.Y. Xia, D. Ye, et al., Herb-functionalized chronic wound dressings for enhancing biological functions: multiple flavonoids coordination driven strategy, Adv. Funct. Mater. 32 (34) (2022).

[35] P. Mehrotra, K.S. Ravichandran, Drugging the efferocytosis process: concepts and opportunities, Nat. Rev. Drug Discov. 21 (8) (2022) 601–620.

[36] A.C. Doran, A. Yurdagul, I. Tabas, Efferocytosis in health and disease, Nat. Rev. Immunol. 20 (4) (2020) 254–267.

[37] S. Maschalidi, P. Mehrotra, B.N. Keçeli, H.K.L. De Cleene, K. Lecomte, R. Van der Cruyssen, et al., Targeting SLC7A11 improves efferocytosis by dendritic cells and wound healing in diabetes, Nature 606 (7915) (2022) 776–784.

[38] H. Wang, Y. Zhang, Y. Zhang, C. Li, M. Zhang, J. Wang, et al., Activating macrophage continual efferocytosis via microenvironment biomimetic short fibers for reversing inflammation in bone repair, Adv. Mater. (2024) e2402968.

[39] J. Yang, X. Zhang, B. Lu, J. Mei, L. Xu, X. Zhang, et al., Inflammation-Responsive hydrogel spray for synergistic prevention of traumatic heterotopic ossification via dual-homeostatic modulation strategy, Adv. Sci. 10 (30) (2023) e2302905.

[40] R. Hanayama, M. Tanaka, K. Miwa, A. Shinohara, A. Iwamatsu, S. Nagata, Identification of a factor that links apoptotic cells to phagocytes, Nature 417 (6885) (2002) 182–187.

[41] W. Cai, X. Dai, J. Chen, J. Zhao, M. Xu, L. Zhang, et al., STAT6/Arg1 promotes microglia/macrophage efferocytosis and inflammation resolution in stroke mice, JCI Insight 4 (20) (2019).

[42] Y. Wang, Y. Lu, J. Lu, P. Hernigou, F. Jin, The role of macrophage polarization in tendon healing and therapeutic strategies: insights from animal models, Front. Bioeng. Biotechnol. 12 (2024) 1366398.

[43] H. Wang, R. Yu, M. Wang, S. Wang, X. Ouyang, Z. Yan, et al., Insulin-like growth factor binding protein 4 loaded electrospun membrane ameliorating tendon injury by promoting retention of IGF-1, J. Contr. Release 356 (2023) 162–174.

[44] A. Fearon, J.E. Dahlstrom, J. Twin, J. Cook, A. Scott, The Bonar score revisited: region of evaluation significantly influences the standardized assessment of tendon degeneration, J. Sci. Med. Sport 17 (4) (2014) 346–350.

[45] P. Saini, M. Arora, M. Kumar, Poly(lactic acid) blends in biomedical applications, Adv. Drug Deliv. Rev. 107 (2016) 47–59.

[46] S. Mondal, S. Park, J. Choi, T.T.H. Vu, V.H.M. Doan, T.T. Vo, et al., Hydroxyapatite: a journey from biomaterials to advanced functional materials, Adv. Colloid Interface Sci. 321 (2023) 103013.

[47] Y. Bi, D. Ehirchiou, T.M. Kilts, C.A. Inkson, M.C. Embree, W. Sonoyama, et al., Identification of tendon stem/progenitor cells and the role of the extracellular matrix in their niche, Nat. Med. 13 (10) (2007) 1219–1227.

[48] J. Li, X. Wang, Z. Yao, F. Yuan, H. Liu, Z. Sun, et al., NLRP3-Dependent crosstalk between pyroptotic macrophage and senescent cell orchestrates trauma-induced heterotopic ossification during aberrant wound healing, Adv. Sci. 10 (19) (2023) e2207383.

[49] S. Chen, Y. Zhou, Y. Chen, J. Gu, fastp: an ultra-fast all-in-one FASTQ preprocessor, Bioinformatics 34 (17) (2018) i884–i890.

[50] D. Kim, B. Langmead, S.L. Salzberg, HISAT: a fast spliced aligner with low memory requirements, Nat. Methods 12 (4) (2015) 357–360.

[51] S. Anders, P.T. Pyl, W. Huber, HTSeq–a Python framework to work with high-throughput sequencing data, Bioinformatics 31 (2) (2015) 166–169.

[52] A. Roberts, C. Trapnell, J. Donaghey, J.L. Rinn, L. Pachter, Improving RNA-Seq expression estimates by correcting for fragment bias, Genome Biol. 12 (3) (2011) R22.

[53] M.I. Love, W. Huber, S. Anders, Moderated estimation of fold change and dispersion for RNA-seq data with DESeq2, Genome Biol. 15 (12) (2014) 550.

[54] M. Kanehisa, M. Araki, S. Goto, M. Hattori, M. Hirakawa, M. Itoh, et al., KEGG for linking genomes to life and the environment, Nucleic Acids Res. 36 (Database issue) (2008) D480–D484.

[55] The gene ontology resource: 20 years and still GOing strong, Nucleic Acids Res. 47 (D1) (2019). D330-d8.

[56] A. Subramanian, P. Tamayo, V.K. Mootha, S. Mukherjee, B.L. Ebert, M.A. Gillette, et al., Gene set enrichment analysis: a knowledge-based approach for interpreting genome-wide expression profiles, Proc. Natl. Acad. Sci. U. S. A. 102 (43) (2005) 15545–15550.

[57] V.K. Mootha, C.M. Lindgren, K.F. Eriksson, A. Subramanian, S. Sihag, J. Lehar, et al., PGC-1alpha-responsive genes involved in oxidative phosphorylation are coordinately downregulated in human diabetes, Nat. Genet. 34 (3) (2003) 267–273.